Max-Planck-Institut
für Meteorologie

REPORT No. 121

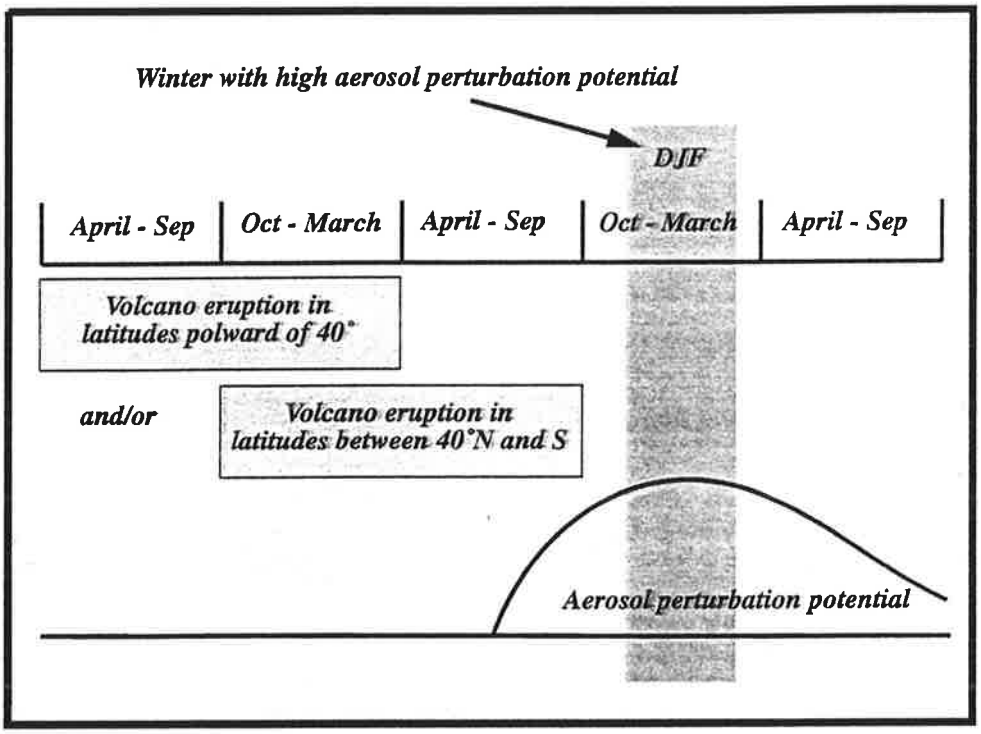

VOLCANOS AND EL NIÑO-SIGNAL SEPARATION IN WINTER

by

INGO KIRCHNER • HANS-F. GRAF

HAMBURG, DECEMBER 1993

AUTHORS:

Ingo Kirchner
Hans-F. Graf

Max-Planck-Institut
für Meteorologie

MAX-PLANCK-INSTITUT
FÜR METEOROLOGIE
BUNDESSTRASSE 55
D-20146 Hamburg
F.R. GERMANY

Tel.: +49-(0)40-4 11 73-0
Telemail: MPI.METEOROLOGY
Telefax: +49-(0)40-4 11 73-298

Volcanos and El Niño - Signal Separation in Winter

Ingo Kirchner and Hans-F. Graf
Max-Planck-Institut für Meteorologie
Bundesstraße 55, D-20146 Hamburg, Germany

Abstract

The aim of this study is the detection of climate signals following violent volcanic eruptions in relation to those forced by El Niño during winter in higher latitudes of the northern hemisphere.

The estimation of potential volcanic climate impact and the El Niño statistics show that the observed effects in high latitudes cannot be clearly assigned to either volcanic or El Niño forcing because of the frequent coincidence of volcanic forcing with El Niño events. In addition, the area covered by observational data is only small. This implies a great uncertainty for the signal selection based only on historical observations. In order to get additional evidence, a set of four different perpetual January GCM experiments was performed (control, volcano case, El Niño case and combined volcano/El Niño case), and studied with advanced statistical methods. The applied statistical methods are a combination of the local t-test statistics and signal detection methods based on Empirical Orthogonal Functions (EOFs).

The amplitudes of the EOF filtered signal for the different forcings are discussed for the temperature field at the surface, at the 850 hPa and at the 50 hPa level heights, for the zonal wind in the 200 hPa and in the 50 hPa level and for the geopotential height of the 500 hPa level. The signal-to-noise ratio analysis shows that the global El Niño signal can be selected more clearly in the troposphere than in the stratosphere because of the signal-to-noise ratio of the El Niño signal is about 20 % stronger in the troposphere than it is in the stratosphere. In contrast, the signal-to-noise ratio of the global volcano signal is strongest in the stratospheric temperature field. For El Niño and volcano forcing statistically significant tropospheric signals occur in different geographical regions. The amplitude of the perturbation for the volcano case is larger in the Atlantic region than anywhere else. The main effect of El Niño forcing is found in the whole tropical region and in mid-latitudes of the North Pacific.

The observed effect of local cooling due to the volcanic reduction of shortwave radiation over large land areas (like Asia) in subtropical regions, the observed advective warming over Eurasia and the advective cooling over Greenland is well simulated in the model. The radiative cooling near the surface is important for the volcano signal in the subtropics, but it is only weak in high latitudes during winter.

The local anomalies in the El Niño forcing region in the tropics, and the warming over North America in middle and high latitudes are simulated as observed. The combination of high stratospheric aerosol loading and El Niño leads to a climate perturbation stronger than for forcing with El Niño or stratospheric aerosol alone. Over Europe, generally the volcanic signal dominates, and in the Pacific region the El Niño forcing determines the observed and the simulated anomalies in winter.

ISSN 0937–1060

1. Introduction

Much of the global climate variability is normally attributed to variations of the El Niño/ Southern Oscillation (e.g. *PHILANDER, 1990*). Facing the violent volcanic eruption of Mount Pinatubo in June 1991, and searching for the climate signal of the increased greenhouse effect, the climate impact of volcanic aerosols becomes more and more interesting. As during the past one hundred years potential volcanic and El Niño effects often coincided (*GRAF, 1986*), it is necessary to separate the various effects of volcanoes and El Niño on climate variability. In order to distinguish the anomaly patterns resulting from such known forcings from the climate background noise, these signals have to be determined from long-term observations or from controlled model experiments.

The atmospheric response to volcanic forcing is part of the natural variability of the climate system as is El Niño. The climate signals of these events must be known so as to be able to determine the effects of anthropogenic climate changes, e.g. of those that are due to the increase of CO_2 emissions. In the present paper, an outline shall be given of the wintertime climate volcanic effects in high latitudes of the northern hemisphere in relation to El Niño response. Since the observational basis is only small for such rare events as violent volcanic eruptions, we use a combination of observational and model studies to extract the climate effects of both factors from the climate background variability.

The globally averaged response of the atmosphere to volcanic activity is cooling near the surface. A detailed analysis by *MASS and PORTMAN (1989)*, based on nine different volcanic episodes, shows different effects on the seasonal global average temperature. The surface air temperature anomalies in their study in most cases are negative after violent eruptions. However, temperature trends after the major eruptions of St. Maria/Mt. Peleé/Soufrieré (1902), Agung (1963) and El Chichón (1982) show warming over the northern hemisphere in some seasons following the eruption. This warming is especially strong during the northern hemispheric winter immediately after the eruption. According to *MASS and PORTMAN (1989)*, the yearly mean temperature signal in some post-eruption years shows a negative sign only for very strong eruptions, with maximum amplitude when a regressive correction is applied for El Niño effects on the temperature records. *BRADLEY (1988)* found the main mean northern hemisphere response (cooling effects) after explosive volcanic eruptions during summer and spring, but he did not detect any measurable effect during winter.

Concerning wintertime surface air temperature effects, *GROISMAN (1992)* as well as *ROBOCK and MAO (1992)* described stable anomaly patterns over Eurasia and North America after volcanic eruptions. *ROBOCK and MAO (1992)* suggested a mechanism according to

which heating of the aerosol-containing stratosphere in lower latitudes results in enhanced westerlies near the polar circle. *GROISMAN (1992)* explained the increased westerlies with intense tropospheric cooling in high latitudes. A new explanation of the middle and high northern hemisphere winter temperature anomaly pattern is given by *GRAF et al. (1993a)*. The basic mechanism underlying the response of tropospheric circulation to tropical volcanic forcing is suggested to be a strengthened stratospheric polar winter vortex resulting from enhanced meridionally differential stratospheric heating by the aerosol-containing layers. The change of the tropospheric planetary wave structure is due to the trapping of planetary wave energy in the troposphere as a result of the strengthened polar night jet. Since changes in the strength of the stratospheric polar winter vortex may occur without volcanic forcing, volcanic aerosol may also just stimulate a natural mode of the stratospheric winter circulation. During winter, in middle and higher latitudes the dynamic response is dominant, thus compensating for the shortwave cooling effect.

The climate response to El Niño in tropical and subtropical regions and its connection with the Indian Monsoon circulation have been described in the literature quite often (e.g. *BJERKNES, 1966*; *HOREL and WALLACE, 1981*; *BARNETT et al., 1991*). The Pacific North America (PNA) Pattern (see *HOREL and WALLACE, 1981*; *von STORCH and KRUSE, 1985*; *HENSE, 1986*) is known as a feature accompanying El Niño events in high latitudes. Such teleconnection patterns in high latitudes, however, cannot be explained with the same plausibility as those in the Tropics. The atmospheric response to El Niño-forcing in higher latitudes of the northern hemisphere, especially in the Atlantic and European regions, cannot clearly be assigned to the tropical sea surface temperature anomalies (SSTA). The impact of SSTA on the extratropical forecast still tends to be very small (*PALMER, 1988*; *SHUKLA and FENNESSY, 1988*).

The changed meridional energy transport during El Niño episodes without doubt affects the planetary wave regime also in high latitudes (*FRAEDRICH et al., 1992*). But, the influence on northern hemispheric wave trains is statistically significant only during winter. *FRAEDRICH et al. (1992)* examined the tropospheric circulation structure of the northern hemisphere during warm and cold extremes of East Pacific equatorial SST anomalies. They investigated a "bimodal distribution" of zonal and meridional circulation types following the classification of circulation types after *DZERDZEEVSKII (1962)*. During warm events the zonal circulation enhanced in high latitudes north of 30°N, and in cold event winters the number of days with zonal circulation types decreased drastically. In the El Niño case in high northern latitudes the persistency of meridional circulation types is shorter than during cold

events. The persistency of zonal circulation is independent of the SST anomaly.

The strong Aleutian Low during El Niño certainly plays an important role in the change of the tropospheric circulation pattern, but the strengthened Aleutian Low also may weaken the stratospheric polar vortex (*LABITZKE and van LOON, 1989*). This is import-ant for climate anomalies in the eastern hemisphere following El Niño (*PERLWITZ and GRAF, 1993*). The volcanic aerosol effects might be able to modulate this El Niño response. Therefore, the strength of the stratospheric vortex can be influenced by both forcings, and an impact on the tropospheric planetary wave patterns is possible (*SCHMITZ and GRIEGER, 1980*; *GRAF et al., 1993a*) via mean flow wave interaction.

It is to be discussed, however, which part of this behaviour is due to the frequently coinciding volcanic and El Niño effects. In the next section, we shall discuss the hypothetical schema of the probable atmospheric response to the volcanic aerosol perturbation after violent volcanic eruptions, and the atmospheric forcing during El Niño episodes including the stratosphere-troposphere interaction. The design of the global circulation model (GCM) experiments and the optimal signal detection methods for analysis of the experiment data are the subject of section 3. The estimated volcanic perturbation potential in combination with the occurrence of El Niño for the past more than one hundred years is described in section 4. We provide a composite of winters with volcanic, El Niño and both factors in relation to unperturbed winters based on the near surface temperature anomalies since 1854. The results of the experiments and the comparison of these signal patterns with observations will be described in sections 5 and 6. A summary of the results is given in section 7.

2. The hypothetical response of volcanic and El Niño forcing during northern winter

The forcing mechanisms of El Niño are different from those of volcanoes. While the forcing during El Niño is a well described positive sea surface temperature (SST) anomaly in the eastern and central tropical Pacific, providing a source of atmospheric moisture and latent heat in the tropics over a well defined area, volcanic forcing is a combination of short- and longwave radiation effects due to the scattering of shortwave and the absorption of longwave radiation at the spatially inhomogeneous distributed volcanic aerosol in the stratosphere. This leads to response patterns varying by regions and seasons.

The warm SST anomalies in the eastern equatorial Pacific that are associated with El Niño are strongly related to the negative phase of the Southern Oscillation (*BJERKNES,*

1966). At intervals of three to five years, these events occur with a lifetime of more than one year. El Niño's atmospheric effects are not only observed on the regional- and global- scale climate, but they also strongly influence the economies of several countries in the Pacific and the Indian Ocean regions (*PHILANDER, 1990*). During El Niño, the tropical ocean-atmosphere system is characterized by weak easterlies in the equatorial East Pacific which in part suppress the upwelling of cold and nutrientrich water in the eastern Pacific. The Walker Circulation cell shifts zonally, obtaining an ascending branch over the central Pacific region. Here the latent heat release increases. The meridional poleward energy transport of heat and momentum also increases.

Via an intensified Hadley circulation, the eddy activities in moderate and higher latitudes are modulated and the wintertime polar circulation in the lower stratosphere is influenced. A warm and weak polar vortex was often observed during El Niño events, but not after strong volcanic events (see *van LOON and LABITZKE, 1987*; *LABITZKE and van LOON, 1989*). Even in the case of an El Niño, the stratospheric polar vortex of the northern hemisphere was strong after the most violent volcanic eruptions (e.g. El Chichón, 1982; Pinatubo, 1991).

As previously suggested (e.g. *GRAF et al., 1993a*), both external forcings - volcanic aerosols and El Niño - do not only directly modulate the tropospheric circulation, but they influence the stratospheric circulation, too. After violent volcanic eruptions periods of high aerosol concentrations one observed in the tropical lower stratosphere, and the strength of the polar vortex increases due to the enforced meridional temperature gradient.

The explosiveness of the eruption and chemical properties of volcanic ejections have a great influence on the strength of climate perturbation. One parameter commonly used to measure the strength of eruptions is the Volcanic Explosivity Index (VEI) after *NEWHALL and SELF (1982)*. Other complex parameters to describe volcanic activity are the Dust Veil Index (DVI) (*LAMB, 1977*) or the Acidity Index (AI) (*HAMMER, 1977*). A survey of the different indices, their benefits and shortcomings is given by *ROBOCK (1991)*. No one of these indices is optimal. They all have specific deficiencies, especially they do not give an objective measure of the SO_2 content of the ejecta, the most important parameter for potential climate effectiveness of an eruption, and the sulfat aerosol concentration as a function of height and latitude.

However, not only the eruption height is of importance, but also the total mass of aerosol-building gases passing the tropopause and reaching the lower stratosphere. The long-term mean global input of volcano-borne sulfur into the atmosphere is estimated to be about 8 % of

the total anthropogenic and natural sulfur input (90 Mt S, *SPIRO et al., 1992*). This value differs widely from year to year, and, in the mean, only about 30 % of the global volcanic sulfur input is produced by eruptions (*BERRESHEIM and JAESCHKE, 1983*). Thus, the atmospheric sulfur from volcanic sources is mainly fed into the troposphere where it has residence times of only one or two weeks.

The longtime mean of the amount of sulfur reaching the stratosphere and contributing to the background stratospheric sulfate aerosol layer is much smaller than the tropospheric emissions. However it can be quite large in single years. For example Mount Pinatubo ejected in June 1991 about 20 Mt of SO_2 into the stratosphere (*BLUTH et al., 1992*; *RUSSELL et al., 1993*). The stratospheric aerosol has residence times of a few years with an e-folding time of the optical thickness of about one year. Stratospheric aerosol, therefore, may induce climate variations during the following seasons in time scales of between one season and some years. *RAMPINO and SELF (1982)* suggested that during 1883-1893 and 1902-1906 the stratospheric optical thickness to a large extent was controlled by sulfur-rich explosive volcanic eruptions.

Several weeks after a violent eruption, additional sulfate aerosol is built in the lower stratosphere due to gas-phase reactions and gas-to-particle conversion from sulfur particles and H_2O (*TURCO et al., 1983*; *PINTO et al., 1989*). The optical thickness increases rapidly during the first months (*REITER and JÄGER, 1986*; *HOFMANN, 1991*). The enhanced stratospheric aerosol reduces solar radiation by scattering and absorption. *WENDLER (1984)* measured an energy deficit of shortwave radiation near ground of 10 W/m^2 in Fairbanks (64°N, 147°W) during the first winter after the El Chichón (April 1982) eruption. The reduction of shortwave solar radiation depends on sun elevation. It is smaller in the tropics than in high latitudes because the sun beams have to pass on increased optical mass at lower sun elevations.

The stratospheric circulation has a strong annual cycle. Stratospheric meridional tracer transport between the tropics and the extratropics mainly takes place during the rearrangement of the seasonal circulation types. The optical thickness (see Fig. 1) were calculated from different sources (Mauna Loa [Hawaii] 19.5°N, 130.4°W; Hampton [Virginia] 37.1°N, 76.3°W; Geesthacht [Germany] 53.5°N, 10.5°E; Obninsk [CIS] 55.0°N, 38.0°E). The data, taken from the Bulletin of the Global Volcanological Network, were normalized to a wavelength of 532 nm. The relation between particle scattering and Rayleight scattering is proportional to λ^3. It is equals one at a wavelength of 308 nm for small particles with radii ≤ 1 µm. Following the Mie theory for such small particles, a linear relationship can be assumend between optical thickness and wavelength. During the months immediately after the eruption in June 1991

the aerosol remained in the tropics (see Mauna Loa, dotted curve in Fig. 1). The optical thickness of the Pinatubo aerosol after June 1991 (Fig. 1) illustrates that the aerosol enters higher latitudes mainly during autumn.

An additional effect is important in the aerosol-containing region. These small particles absorb longwave terrestrial radiation and, thus, the lower stratosphere is heated with the largest effects in the tropics. So, *GOBBI et al. (1992)* measured a heating rate of 2.5 K/month in middle latitudes and in 20..25 km altitude during autumn 1991 after the Pinatubo eruption. *LABITZKE and NAUJOKAT (1983)* observed anomalies of 4-5 Kelvin in 30 hPa and 50 hPa from July to November 1982 after the El Chichón eruption in the tropics. Similar values were reached after the Pinatubo eruption (*GRAF et al., 1993b*).

Thus, volcanic aerosol reduces the shortwave energy input near the earth surface, and it changes the meridional temperature gradient in the stratosphere. The El Niño effect, however, consists mainly of an additional latent heat source in the tropical troposphere. The enhanced stratospheric meridional temperature gradient may lead to a strengthening of the polar night vortex. Linear theory of atmospheric mean flow/wave interaction suggests that a strong polar vortex reflects the vertically propagating energy of tropospheric planetary waves back to the troposphere and, thus, alters the standing wave pattern in the troposphere (*MATSUNO, 1970*; *GELLER and ALPERT, 1980*). The standing wave pattern associated with the strong stratospheric polar vortex produces westward wind anomalies over the North Atlantic (*GRAF et al., 1993a*).

Thus, the winter anomalies in higher latitudes do not only depend on the direct tropospheric effect of reduced solar radiation or of tropical latent heat excess. They depend also, and possibly in the same magnitude, on the changes of the stratospheric circulation. Because of the indirect dynamic forcing due to the stratospheric circulation this signal is strongest in the upper troposphere and smaller in the lower troposphere.

3. Four perpetual January experiments

3.1. The model calculations

In the present study we used the T21 version of the ECHAM2 GCM with the physical parameterization scheme described by *ROECKNER et al. (1989)*, *CUBASCH (1991)* and in *DKRZ-Report 6 (1992)*. The uppermost of the 19 levels is at 10 hPa, and the triangular truncation by a wavelength of 21 provides a horizontal resolution of about 5.6 degrees. The time step is 40 minutes. The internal radiation scheme of the ECHAM2 climate model, which uses a cli-

matologically prescribed aerosol distribution, has been extended by using the "anomaly forcing" technique where an additional sophisticated radiation model *SCHULT (1991)* calculated the aerosol effects explicitly (*GRAF et al., 1993b*). The radiation transport equation is solved with the δ-Eddington approximation (*BAKAN, 1982*). The aerosol parameters were adapted from observations after the El Chichón (1982) and Pinatubo (1991) eruptions. The model is calculated in parallel with the original ECHAM2 radiation code, once with and once without the prescribed aerosol and with the atmospheric conditions from the climate model. The flux differences of the two δ-Eddington computations are then added to the results of the original code. After six months of computation we obtained stable mean monthly anomalies of the radiative fluxes and heating rates. The effect of aerosol longwave radiation on the surface radiation balance is more than one order of magnitude less than the total effect and has been neglected in the volcano forcing computations.

The computed heating rates in the lower stratosphere, and the shortwave radiation effect near ground for January conditions of the first winter after a violent tropical eruption were then used to force the climate model for all volcanic forcing experiments.

All integrations were performed in the perpetual January mode with daily cycle. The atmospheric conditions of the Nth January 30 were used to initialize the (N+1)st January. With this scheme, the GCM was integrated over 60 Januaries for each of the four experiments (CTRL, VOLC, EN, VOEN). The reference experiment (CTRL) is running with climatologically prescribed sea surface temperature and without additional aerosol forcing.

The second experiment is the volcano case, VOLC (see *GRAF et al., 1993b*). The boundary conditions are the same as in the control. External heating rate anomalies (see Fig. 2, upper panel) were added in the stratosphere, i.e. to the upper six model levels. These heating rates were derived from the anomaly forcing experiment with the additional aerosol radiation transport model and for an El Chichón/Pinatubo type aerosol for January 1983 and 1992, respectively. The shortwave radiation reduction effect was simulated with the reduction of the solar radiation at the top of the model atmosphere according to the above calculations. This volcanic forcing combines the surface cooling effect and the heating in the aerosol layer region.

Our aerosol heating rates are in good agreement with the estimations of *KINNE et al. (1992)* for a Pinatubo aerosol. The modelled radiation effects of a similar aerosol, as computed with a radiative-convective model by *LACIS et al. (1992)* for the El Chichón aerosol for global mean conditions, give a net radiation flux reduction at the tropopause of 3.3 W/m^2 one month after the eruption and of 2.5 W/m^2 after 6 months. The equilibrium temperature in the strato-

sphere increases by about 3 K in the case with an additional aerosol layer in the altitude of 15-20 km. Our shortwave radiation effect is in the order of 5 to 12 W/m^2 (see Fig. 2 bottom).

The third experiment (EN) is for the El Niño case. The atmospheric model conditions are the same as for the CTRL experiment, but the surface conditions have been changed. The sea surface temperature anomalies in the area between 25°N and 25°S, as observed in January 1983, were added to the mean sea surface temperature (Fig. 2, middle panel).

In the fourth experiment (VOEN), the El Niño experiment boundary conditions were combined with the heating rates and the shortwave radiation reduction corresponding to the volcano experiment.

The average surface solar net fluxes for all experiments (Fig. 2, lower panel) illustrate the dominance of the radiation forcing in higher latitudes in the volcanically perturbed experiments (especially in the summer hemisphere), and of the cloud effects in the tropics in the El Niño experiments.

To check for the reliability of perpetual January simulations, we compared the mean model climate as computed in the perpetual January mode with that of the mean January of the 20-year transient (i.e. full annual cycle) control run of ECHAM2. The basic features of the model climate of both Januaries are similar in midtropospheric circulation and in surface air temperature. Of course, there are some differences, but in most cases they are in the range of model variability. In particular, there were no trends detected, though it seems that the perpetual January runs slightly favour the strong polar vortex mode. But, since our studies are based on anomalies, any systematic errors are expected to be filtered out.

3.2. Signal selection technique

We applied a variety of statistical methods to extract the model's response to the experimental forcing (signal) from the model climate (noise). Fig. 3 schematically shows the different parts of this analysis. At first we used the local t-test to analyze the differences between the three forcing experiments (Volcano, El Niño, and both) and the control run. This technique is described in Appendix 2.

The temporal dimension for the experiments and for the reference run is 58. In the case of perpetual January experiments we found stationarity for all forcings. A certain trend in the experiment data exists only in the first few months. These months had been truncated before the analysis was started. We only investigated monthly means.

The effective number of degrees of freedom was calculated from the autocorrelation func-

tion, using the Bartels' number B (see in TAUBENHEIM, 1974) which varied between 1 and 2 months over most of the grid points for all meteorological parameters in our experiments. Only in regions south of 80°S this number is larger than two. As a conservative estimate for the local t-test we used a $B = 2$, to estimate $n_{e,c}/B$ (equals 29) as the effective number of degrees of freedom for all grid points.

The statistical significance of the t-test value depends on the numbers of independent ensembles. With increased number of realizations, the local t-test statistics gives statistical significance without a physical background. With the recurrence test (*von STORCH and ZWIERS, 1989*), the difference between the distributions of the control and the experiment parameters is analyzed, and only physically meaningful differences between the control and the experiment state reach the significance level. In all our experiments, areas showing anomalies significant by the local t-test with a confidence level of 99% are consistent with areas having a 84% recurrent signal. The difference between the experiment mean and the model climate is larger than two standard deviations in this case (*von STORCH and ZWIERS, 1989*).

Both methods, local t-test and recurrence analysis, do not give any signal in regions with large natural variability. The average signal is overlaid by the internally produced climate noise. Our external forcing may enhance only few dimensions in the multidimensional phasespace of the climate system. These few dimensions can be determined with signal detection methods based on Empirical Orthogonal Function (EOF) analysis in the climate system (see e.g. *HASSELMANN, 1992*; *SANTER et al., 1993*). We use this technique to filter the volcano and the El Niño signals from noise in our experiments.

We estimated the signal-to-noise ratio for six different meteorological parameters. We want to concentrate our analysis on the zonal wind in the 50hPa and the 200hPa levels, the geopotential height of the 500hPa level, the temperature in the 50hPa and the 850hPa levels, and on the surface air temperature. All used fields are area weighted anomaly data relative to the mean of the control run.

In our case, the spatial dimension is 2048, and we have 57 basis vectors in each EOF set. The covariance matrices used for computing the EOFs are rank-deficient (see *PREISENDORFER, 1988*), so that the number of EOFs with non zero eigenvalues is actually 57. The estimation of the EOFs is limited by the ratio of the number of temporal to the number of spatial dimensions.

We applied a Monte Carlo (MC) estimation of the objective information potential (see Appendix II). The number of basis vectors derived from the MC estimation is smaller than the

number of EOFs describing 95% of total variance, a level used e.g. by *SANTER et al. (1993)*. Avoiding non resolvable information, we only give the results according to the MC estimation of meaningful EOFs as a measure of the signal-to-noise ratio.

The variations of the Principle Component time series (PC) with time are secondary because we are interested in the mean signal amplitude. Thus, we compared the time average of each experiment $PC_{e;EOFe}$ with the corresponding $PC_{c;EOFe}$ of the control case and with the signals based on an ensemble of mixed data sets following the procedure described in Appendix II, part 3. The reference EOFs in this analysis are the experiment data EOFs. In first order, we calculate the t-test statistics (e.g. *DAVIS, 1973*) and we select only basis vectors with a statistical significance of more than 99%. Because the Student's t-test of the average PC amplitudes is not powerful enough in this case, we calculate an additional Monte Carlo statistics (see Appendix 2).

4. Relations between volcanic activity and El Niño based on observations

In this section, we want to quantify the influence of volcanic activity on climate in relation to El Niño activity on the basis of observations. The main problem to solve is that there are not enough data available. Not all important features of volcanic activities are measured over a time range long enough to apply statistical techniques. Information on eruption height (VEI), total aerosol loading (DVI), geographical position and season of the eruption were therefore used to generate a table of volcanic events of high climate perturbation potential (see Appendix 1). The term "potential" is introduced here because only in few cases we have information on the sulfur content. Only a high perturbation potential plus a high sulfur content make the climate impact of an eruption possible. Different sources were utilized to classify the eruptions (*SIMKIN et al., 1981* update 1991; *BERRESHEIM and JAESCHKE, 1983*; *ASATUROV et al., 1986*; *ROBOCK, 1991*).

All known volcanic eruptions which occurred during the past centuries have been listed and classified for their VEI by *NEWHALL and SELF (1982)*. The VEI is important in so far as it includes an estimated height of the eruption column. Eruptions exceeding VEI = 3 most probably have reached the stratosphere. Our volcano table, in accordance with the study of *ROBOCK and MAO (1992)*, contains volcanic eruptions with a VEI = 4 or more and/or a DVI greater than or equal to 200. A climate signal of volcanic aerosol is only detectable in the months or seasons following these eruptions. During these periods a high volcanic perturbation potential exists. A comparison of the volcanoes listed in Appendix 1 with SO_2 TOMS esti-

mates since 1979 (see KRUEGER in *AGU, 1992*) shows that only about half of the eruptions classified as potentially climate-influencing had ejected SO_2 amounts of more than one Megaton. Thus, the number of climatically effective eruptions used here is overestimated, giving rise to an underestimation of the observed volcanic climate signal.

The volcanic effects on climate are expected to be sensitive to the season of the eruption and to the latitude of the volcano. Therefore, the combination between the location and the eruption date was also considered in the classification scheme (Fig. 4). The volcanic events were subdivided into those at locations in latitudes poleward of 40°N or S and those between 40°N and 40°S.

During the first winter following a low latitude eruption, according to observations after the El Chichón and Pinatubo eruptions (compare with Fig. 1) the volcanic perturbation potential is maximal in the tropics. The distribution of the volcanic aerosol after higher latitude eruptions is not as clear. Two rearrangements of the stratospheric circulation were considered to be necessary to move a substantial part of the injected aerosols to the tropical stratosphere. We suggest that not until the second winter following an eruption polward of 40° the volcanic perturbation potential reaches it's maximum in the tropics. The climatic effect of high-latitude eruptions is expected to be much smaller than that following low-latitude eruptions since, after such a long time, the maximum aerosol loading in the stratosphere has already passed.

The description of El Niño activity is much simpler in relation to the quantification of the volcanic influence. A good parameter to describe this phenomenon is the Southern Oscillation Index (*BJERKNES, 1966*), or the sea surface temperature (SST) anomalies in the tropical East Pacific (*WRIGHT et al., 1989*). In our study we compared the El Niño events based on the SST index with El Niño listed by other authors (*NAMIAS, 1976*; *QUINN et al., 1978*). The winters since 1850 that had been influenced by a warm event are 1850/51, 1852/53, 1854/55, 1855/56, 1857/58, 1862/63, 1866/67, 1868/69, 1871/72, 1873/74, 1875/76, 1876/77, 1877/78, 1880/81, 1884/85, 1885/86, 1887/88, 1888/89, 1895/96, 1896/97, 1899/1900, 1900/01, 1902/03, 1904/05, 1905/06, 1911/12, 1913/14, 1914/15, 1918/19, 1923/24, 1925/26, 1930/31, 1939/40, 1940/41, 1941/42, 1944/45, 1951/52, 1953/54, 1957/58, 1958/59, 1963/64, 1965/66, 1968/69, 1969/70, 1972/73, 1976/77, 1977/78, 1982/83, 1986/87, 1987/88 and 1991/92.

Both data sets, the volcanic potential impact estimation and the El Niño statistics, were used to separate winters into four different classes: one with high volcanic perturbation potential, one with warm SST anomaly, one with both factors, and one without volcanic or El Niño forcing. Following this classification, from 1850 to 1990 there were twenty-five winters with

El Niño forcing, 26 winters with high stratospheric aerosol loading potential, and 25 winters with a combination of El Niño and volcanic forcing. Sixty-four winters without El Niño or volcanic perturbation were classified from 1850 to 1990.

The relation between these classes as a function of time in twenty-year periods is shown in Fig. 5. The fraction of volcano-perturbed winters, volcano- and El Niño-perturbed winters and single El Niño-forced winters is about 20 % each of all the 140 analyzed winters. The part without any forcing is 45 % of all winters, not only for the whole period but also for nearly all twenty-year subperiods, except for a small disturbance before 1890. The distribution of volcano-perturbed periods and El Niño-perturbed periods suggests that the volcanic (El Niño) response in 50 % of the observed cases available is disturbed by El Niño (volcano) effects. On the other hand, the atmospheric response of 50 % of the strongest eruptions (indicated by stars in Fig. 5) is perturbed by the atmospheric response of El Niño.

This illustrates the statistical problem encountered when attempting to separate the signal of El Niño from the volcanic effects, if only observations are used. The observed effects in high latitudes cannot clearly be assigned to volcanic or El Niño forcing because the sample with high potentially volcanic aerosol loading without El Niño is only about 20 % and, on the other hand, the sample with El Niño forcing without high stratospheric aerosol loading potential is also only about 20 %.

Despite the difficulties described above, the volcano/El Niño classification was used as the basis for a superposed epoch analysis of the global data set of surface air temperature (*JONES et al., 1986*, update 1992). The horizontal resolution of this data record is 5° latitude times 5° longitude. At many grid points, data exist only for the last few years. This can provoke a failing of the results (e.g. in case of any trends in the time series). Fig. 6 shows the differences between each perturbed class and the unperturbed winters. The shaded areas are regions with significant anomalies exceeding the 99 % confidence level using the local t-test. In the El Niño perturbed winters (single and in combination with volcanic forcing), the SST anomaly dominates the response in the tropics, and over North America the positive signal increases in strength in the case without volcanic forcing. A volcano signal is detectable only in a small area of Asia, where significant positive surface air temperature anomalies are found. An independent analysis (*ROBOCK and MAO, 1992*) of the same data set only for the 12 strongest eruptions and with regressive elimination of the El Niño effect shows the same anomaly patterns as in our winters classified as volcanically disturbed, especially concerning the warming over Eurasia and North America and the cooling in the Greenland region.

The observed anomalies in high latitudes can be explained by the linear mean flow/wave interaction theory (*GRAF et al., 1993a*): Differential heating of the stratosphere between low and high latitudes leads to a stronger polar stratospheric vortex which, by trapping vertically propagating planetary wave energy in the troposphere, affects the tropospheric planetary wave pattern.

A composite of months with strong and weak stratospheric vortexes was performed for the period from 1957 to 1992 (*GRAF et al., 1993a*). Fig. 7 shows the difference between the surface air temperature anomaly patterns of months with strong (upper panel) and weak vortexes (lower panel), respectively, in relation to all unperturbed months. Classifications as strong and weak vortex months is based on radiosonde observations of geopotential height of the 50 hPa level by *LABITZKE (1992)* since 1957, as analyzed in the EOF (Empirical Orthogonal Function) space by *PERLWITZ (1992)*. The stratospheric data are monthly means in a 10° times 10° resolution, with the annual cycle being removed.

The comparison of the pattern forced by the strengthened stratospheric vortex with observations during high aerosol loading potential periods clearly indicates the association between the strength of the polar vortex and the volcanic climate response. Positive wintertime temperature anomalies over northern Eurasia are a feature of months with strong stratospheric vortex (Fig. 7) and also of winters with high stratospheric aerosol perturbation potential (upper panel in Fig. 6). After the volcanic eruptions without coincidence of El Niño (Fig. 5), the anomalies over Eurasia have amplitudes smaller than those associated with a strong vortex, because the very strong eruptions took place in conjunction with El Niño's and were, therefore, not included in the "volcano" but in the "volcano + El Niño" category.

This simple analysis of observational data reveals two important facts:

(1) The most violent eruptions occurred together with El Niño events (see Fig. 5), and a relatively small aerosol perturbation potential occurs in periods following volcanic eruptions not accompanied by El Niños. Therefore, the analyzed volcanic effect (Fig. 6, upper panel) is only small.

(2) The area covered by sufficient data is restricted to the continents. This implies great insecurity when studying the global mean volcanic effect. Large regions with a significant signal are found only for the El Niño cases (see Fig. 6).

Because of the limited data available of only volcanically perturbed winters, the results are statistically not very striking (see the shaded areas in Fig. 6). Any more sophisticated signal detection strategy, e.g. in the EOF domain, is also not practicable because of the weak

observational data basis. Extraction of the El Niño-dependent part of the climate signal by just applying a linear regressive filter seems not to be a prior justified, since it is not sure that the combined forcing of volcanic aerosol plus the El Niño type SST anomaly would lead to a linear combination of the single responses. Therefore, we performed a set of four different series of perpetual January GCM experiments to study the influence of volcanic aerosol on climate separated from the El Niño effects. The results of these experiments will be discussed in the next section.

5. Results of perpetual January experiments

5.1. Local anomalies

In the El Niño and in the volcano experiments, the strongest anomalies from the undisturbed model climate were found in the geopotential and wind field of the upper troposphere. Fig. 8 shows the local t-test results (shaded areas indicate statistical significance of 99 %) of the zonal wind anomalies from the control experiment in the 200hPa layer for experiments VOLC, VOEN and EN. The experiments result in statistically significant anomalies at different areas for different forcings.

In the volcano case (top panel), a characteristic pattern occurs over the Atlantic region: The westerlies near the tropopause increase in high latitudes, while an easterly wind anomaly occurs in middle latitudes. A similar pattern, but with smaller amplitude, exists over the northeastern Pacific.

The El Niño response (bottom panel) in 200 hPa is characterized by an easterly wind anomaly over the whole tropical Pacific region and by westerly anomalies over the tropical Atlantic, extending across Africa to the Indian Ocean and Indonesia. Westerly anomalies in the subtropics and weak easterly anomalies in high latitudes are prominent over the North Pacific region. This, in the Pacific region, is just the inverse pattern of the one of the volcano experiment (Fig. 8, top panel). No El Niño signal is detectable over the North Atlantic.

The experiment with both forcings (Fig. 8, middle panel) reproduces the tropical Pacific anomalies like in the El Niño experiment. The anomalies in higher latitudes, especially over the Atlantic, are much smaller than in the volcanic case, and the local t-test indicates no significant amplitudes.

The significant temperature anomalies in the lower troposphere are concentrated on the tropics in the El Niño experiment (Fig. 9, bottom panel). The area of positive sea surface tem-

perature anomalies over the eastern tropical Pacific is clearly indicated, and this applies also to the warm anomaly over Australia. The only large-scale extratropical temperature anomaly occurs over the northwestern part of North America. This is in agreement with annual cycle model experiments of other authors (e.g. *CUBASCH, 1985*).

In contrast to the El Niño experiment, in the volcano case the strongest anomalies appear in high latitudes, mainly over the North Atlantic and Eurasian areas. These anomalies are due to changes in the planetary wave patterns (see *GRAF et al., 1993a*). The negative temperature anomalies over northeastern North America, the Davis Strait and Greenland are due to cold air advection in connection with the trough developing in that area. The warm anomalies over the northern part of Eurasia result from warm and moist air being advected by the enhanced Atlantic westerlies. As a result of the reduction of short wave radiation in northern hemisphere subtropics, weak, but locally significant negative temperature anomalies are seen in the Mediterranean, the Middle and the Far East. In the eastern Mediterranean this cooling is also due to cold air advection at the eastern flank of the positive pressure anomaly developing over Europe.

For combined volcano and El Niño forcing, the El Niño part of the signal remained stable, while the volcanic signal over northeastern North America is weaker, as is the Mediterranean cold anomaly. The area of the warming in very high latitudes of Eurasia is extended in the case of combined forcing.

According to the local t-test, there exist locally significant anomalies for all experiments. The question is whether these anomalies are physically meaningful or whether they are significant simply due to the large number of realizations. Therefore, we also applied a recurrence analysis (*von STORCH and ZWIERS, 1989*). This test confirmed our t-test results, suggesting that the local anomalies discussed above (Figs 8 and 9) are real ones, i.e. the distribution functions differ significantly between the experiments and the control run.

5.2. The signal-to-noise ratio

Now we shall investigate the patterns underlying these signals, and the signal-to-noise ratio for different parameters in order to find an optimized signal. This analysis was performed following suggestions of *HASSELMANN (1992)* and *SANTER et al. (1993)* to filter experimental and model climate data using EOFs as described in Appendix 2.The results of this analysis are given in Table 2 of Appendix 3.

The first column of Table 2 determines the parameters n_{MC} (number of meaningful EOFs), $V^{nMC}{}_{ref}$ (explained variance for projection of control [experiment] run data onto meaningful

control [experiment] EOFs), V^{nMC} (explained variance for projection of experiment [control] run data onto meaningful control [experiment] EOFs), and the ratio between $V^{nMC}/V^{nMC}{}_{ref}$, an estimate of the signal-to-noise ratio.

The differences $\delta V^{nMC}{}_{ref}$ and δV^{nMC} between the control data and the experiment data analysis are an indication of the error of estimation. The difference between the projection of the experiment data and the control data onto one and the same set of EOFs ($V^{nMC}{}_{ref}$ and V^{nMC} of the control [experiment] data) is a measure of the orthogonality between signal and noise (climate). This difference should be larger than the error of estimation in order to be able to detect any signal. As becomes clear from the figures in Table 2 for the projections of the experimental and control data onto the respective EOF sets, the error of estimation of explained variance for δV^{nMC} is in the order of 10%, and about 2 % for $\delta V^{nMC}{}_{ref}$.

From the analysis based on Monte-Carlo simulations follows that, in the mean, 84-88 % of the total variance of the studied data sets can be explained by meaningful EOFs. The remainder is white noise and nonresolvable information. This means that using the common 95%-rule (e.g. *SANTER et al., 1993*) the amount of resolvable information is overestimated.

As a rule, the data are very noisy (i.e. the spatial correlation is small), if the number n_{MC} of meaningful EOFs determined from the projection of a data set onto one EOF set is large. In this case, the ratio of V^{nMC} to $V^{nMC}{}_{ref}$ does not contain useful information about the signal-to-noise ratio. On the other hand, the potential to detect a signal is high in the case of few degrees of freedom (small number of n_{MC}) and orthogonality between signal and noise ($V^{nMC}/V^{nMC}{}_{ref} << 1$). An intercomparison of the estimated orthogonality of signal and climatic noise between the different experiments shows that this parameter improves in the troposphere for the experiments with El Niño forcing.

The estimated orthogonality between signal and climatic noise is small for all parameters under investigation. The highest estimate of orthogonality between signal and noise is found for the parameter of zonal wind in the 200 hPa level. Here the ratio of V^{nMC} divided by $V^{nMC}{}_{ref}$ is about 0.5. On the other hand, the number of estimated meaningful EOFs (n_{MC}) is largest for this parameter, indicating strong noise.

Our model data are characterized by very close space-time correlation in the stratosphere, as can be seen in Table 2 for temperature and zonal wind in the 50 hPa level. The weakest space-time correlation occurs in the zonal wind field of the 200 hPa level. There are no obvious differences in the space-time correlations between the experiments, except for the stratospheric temperature in all experiments forced by volcanic aerosol. Here n_{MC} is 4. The param-

eter n_{MC} has small values for the volcanically forced experiments only for the temperature in the 50 hPa level. This is the direct result of external forcing.

Generally, the chances for signal detection on the basis of variability are expected to be only small for this type of forcing, because the pattern of the possible signal corresponds with one or more patterns of inherent variability. In the next section, we therefore investigate the differences between the experiments on the basis of the amplitudes of these patterns.

5.3. The global signal amplitudes

In this section, the amplitudes of the meaningful EOFs of the experiments are compared with those of the control run, using the projections of the control and experimental anomalies onto the experimental EOFs as described in Appendix 2, part 3. All analyses are based on global arrays. The restriction of analysis to the northern hemispheric data does not produce notable differences in the patterns.

An overview of the results is given in Table 3 for the volcano experiment, in Table 4 for the combined experiment, and in Table 5 for the El Niño experiment. These tables include all EOFs that are different with a significance level of 99 % following Student's t-test. The rank of the EOFs is given in the first column and the explained variance of these EOFs is shown in the second one. The third column is the time average of the PC. Columns four, five and six give the results of the MC amplitude test, using different significance levels. The number of random subsets, unlike the justified significant level in relation to the experiment PC (see Appendix 2), is given relative to all random subsets as a measure of the strength of the experiment signal. In Table 6, the global analysis is compared with the northern hemispheric analysis (30°N - 80°N).

It becomes obvious from Tables 3 to 5 that the global volcanic signal, though statistically significant, is weaker than the El Niño signal in the troposphere (especially in the lower troposphere). The opposite holds for the stratospheric response of temperature and zonal wind in the 50hPa level for the global analysis.

In the stratosphere, the EOF filtered signal is determined by volcanic forcing. In the volcano experiments, the first EOF of the temperature field in the 50 hPa level explains more than 80 % of the total variance. In the El Niño experiment, the stratospheric signal is distributed over two EOFs, explaining only about 40 % of the total variance (Fig. 10, bottom). The northern hemisphere analysis shows no signal for the El Niño case in the stratospheric temperature. From Fig. 10 it becomes evident that volcanic forcing leads to the expected warming of the tropical stratosphere, while it cools the stratosphere over very high northern latitudes.

In contrast to the volcanic forcing, the warm SSTs of the El Niño case lead to a zonally symmetric cooling of the tropical stratosphere and to the formation of a wave number one pattern in higher latitudes with a warming over the northern Pacific and cooling over the North Atlantic. This pattern corresponds with the observations of *LABITZKE and van LOON (1989)* in El Niño winters. The stratospheric effects due to the El Niño forcing of the model are about ten times smaller than those resulting from volcanic forcing (see column 3 in Tables 3 and 5). Thus, in the case of combined forcing the volcanic effect dominates in the stratosphere.

The differences in explained variance between the experiments are smaller than those for the temperature field in case of the zonal wind field of the 50 hPa layer (Fig. 11). After a violent volcanic eruption, the northern hemispheric polar winter vortex is strenghtened. A strong maximum is observed over the North Atlantic, and a secondary maximum is over the Bering Strait. In the El Niño case, the strongest signal in the zonal wind field of the 50 hPa layer occurs over the Pacific. It consists of negative anomalies in the tropics, positive ones in the subtropics, and a weak polar vortex in high northern latitudes. In the combined experiment (VOEN), the positive anomalies are shifted somewhat towards the south as compared to the volcano experiment (VOLC).

The volcanic signal, which is strong in the stratosphere, becomes weaker in the troposphere, as compared with the El Niño signal in the zonal wind field. In the 200hPa level, the volcano signal in the zonal wind field, which is clearly restricted to the North Atlantic, explains only half as much of the total variance as does the El Niño signal (Fig. 12). In the El Niño case, in the tropical upper troposphere easterly anomalies dominate over the Pacific and westerlies are found from the Atlantic crossing Africa to the Indian Ocean. Westerly anomalies occur in the Pacific subtropics. In the combined experiment, the El Niño signal dominates the zonal wind field. It explains more variance than in the other experiments.

The volcano signal of the geopotential field of the middle troposphere (Fig. 13) behaves similar to the zonal wind field in the 200 hPa level. It is strongest over the North Atlantic, with a trough developing over Greenland and a positive geopotential anomaly between 40°N and 60°N in mid latitudes. Weaker positive anomalies are found over Alaska and North Siberia, where the amplitude is even smaller but the area is larger. Zonally symmetric positive values in the tropics are characteristic of the signal in the geopotential field of the 500 hPa layer for the El Niño case, as are a strong negative anomaly over the North Pacific and positive values over North America. For combined forcing, the El Niño signal remains dominant in the tropics and in middle and high latitudes. But, a modified volcano signal is clearly formed from the Atlantic to northern Eurasia. The trough over Greenland is weaker in VOEN than in

VOLC, and the positive anomaly visible in the volcano experiment over the North Atlantic (Fig. 13, top) is also smaller. The Greenland trough is embedded into a large-scale band of positive geopotential anomalies reaching from the West Coast of North America to central Siberia in mid and high latitudes.

In the lower troposphere, the dynamically enforced part of the volcano signal is still weaker and the effect of the reduction of shortwave solar radiation becomes increasingly visible over the continental subtropics (Fig. 14). The cooling effect over Greenland and the strong warming over northern Eurasia are the result of advection of cold and warm air masses, respectively. In contrast to this pattern, in the El Niño case strong temperature anomalies are formed in high latitudes only over the northwestern part of North America.

The EOF filtered volcano signal (sum of the three significant patterns, see Table 3) of the surface air temperature (Fig. 15) explains more variance than the El Niño signal does. However, the difference between the amplitude of the volcano signal and the climatic noise is much less than for the El Niño signals (VOEN, EN). Analysis of only the northern hemisphere gives a stronger signal for the lower tropospheric temperature for the volcanic case than for the El Niño experiment.

6. Comparison of the experiments with observations

In this section, we are going to compare our modelled results with observations. Because of the limited availability of homogeneous global or hemispheric data sets, we selected three cases which are comparable with our experiment settings. The case study winters have been chosen as follows:

(a) Matching our EN experiment settings, in the winter of 1986/87 a strong El Niño occurred without global stratospheric aerosol disturbances. Although in the spring of 1986 the volcanoes Augustine and Pavloff erupted on the Aleutian Islands, they did not produce widespread stratospheric aerosol perturbations.

(b) The volcano experiment VOLC was compared with the winters of 1974/75 (the winter with a strong polar vortex and the minor volcanic eruption of Fuego in Guatemala) and 1991/92, the winter after the very strong Mount Pinatubo eruption (20 Mt of SO_2, *BLUTH et al., 1992*). A moderate El Niño occurred also during 1991/92, but its influence is expected to be only minor in comparison with the strong volcanic disturbance.

(c) Finally, matching our VOEN experiment settings, the winter of 1982/83 was influenced

by the very strong El Niño 1982/83, and the stratospheric aerosol layer was perturbed by the aerosol produced from the ca. 7 Mt of SO_2 ejected into the stratosphere by the El Chichón eruption of April 1982 (*KRUEGER, 1983*).

For the free atmosphere we used observations of the monthly means of the geopotential heights of the 500hPa level north of 20°N. These data are based on the analysis of the National Meteorological Centre (NMC) of the U.S. Weather Service and were transformed to a 5° times 5° grid at Max-Planck-Institut für Meteorologie.

Further, we investigate the temperature anomaly patterns at the lower troposphere and the surface air temperature data of *JONES et al. (1986)*, extended up to 1992. Long-term global data sets are available only for surface air temperature. For the temperature field in the lower troposphere we use the NMC temperature data of the 850 hPa layer (available from October 1962 to June 1989) and the Microwave Sounding Unit (MSU) data set (*SPENCER and CHRISTY, 1991*) (this globally homogeneous temperature data set is available as from 1979) to compare the simulated temperature anomalies with observed anomalies in the lower troposphere. We suggest that the free troposphere data are more comparable with the experiment temperature signal in 850 hPa than are the near surface temperature anomaly data (*JONES et al., 1986*), due to (1) mainly large-scale dynamic processes being responsible for the anomaly patterns in the lower troposphere, and (2) the strong local influences of the climatology prescribed sea surface temperature and ice mask in higher regions overlaying the patterns.

At first, the observed and the EOF filtered modelled 500hPa layer geopotential height anomalies are discussed for the El Niño case (Fig. 16). A negative anomaly in the Aleutian region occurs in all El Niño cases, and features of the PNA pattern are visible. Large differences between observations and model are visible over the Atlantic and Eurasian regions.

The lower troposphere temperature pattern of the El Niño case (Fig. 17) is dominated by a strong positive anomaly over North America in observations as well as in the model simulation. The observed pattern over Eurasia does not match the model result. The observations show strong negative anomalies, while positive anomalies were calculated over the Eurasian continent. We suggest that this is due to the model's lacking ability to essentially disturb the stratospheric vortex. Therefore, the planetary wave patterns over the Atlantic and Europe are not influenced.

A strong positive geopotential height anomaly over the East Atlantic and West Europe, and a strong negative anomaly over Greenland occur in case of a volcanic aerosol perturbation

(Fig. 18). In the El Niño case (Fig. 16), the signs were reversed: the positive anomaly was seen over Greenland (only in the model) and a negative one over Europe.

The comparison of the 850hPa level temperature experiment signals with the observations shows reasonable similarity in the volcano case and in the mixed case. In the volcano case during winter, the temperature (Fig. 19) over the North Atlantic and northern Eurasia is warmer than normal and cold air is advected from the polar regions towards Greenland. The shortwave radiation effect in the volcano case is detectable only in lower latitudes, as over Southern Asia and North Africa.

In the literature, studies concerning volcanic impact on climate normally use only the near surface air temperature. As suggested above, this may not be the optimum parameter for the comparison with model results. The model signal-to-noise ratio is stronger for the temperature in 850 hPa (see Appendix 3, Table 2) than for the surface temperature. The EOF filtered signal (see Fig. 15) of the surface air temperature anomaly generally shows the same features as in the 850 hPa level, except in very high latitudes where the model's prescribed ice mask prevents the occurrence of anomalies. In subtropical regions, the effect of reduced shortwave radiation is much stronger in the surface air temperature than in the free troposphere, but in middle and higher latitudes circulation controls the temperature structure. North Asia and the West Coast of North America are warmer, and the East Coast of North America is colder than normal. This feature was also observed by *SPIRINA (1973)*, *GRAF (1986)*, *LOUGH and FRITTS (1987)*, *SEAR et al. (1987)* and *GROISMAN (1992)* after strong volcanic eruptions, and this is just the temperature pattern which was observed during the winters of 1991/92 and 1992/93 after the Pinatubo eruption.

The comparison of the modelled (Fig. 15) and observed (Fig. 6) surface air temperatures does not show as much similarity as for the free troposphere. Beside the above suggestions, an additional reason may be the small data density over large areas of both hemispheres. If only the areas with very strong amplitudes are considered, the basic similarity between simulations and observations, nevertheless, becomes more evident.

The combined El Niño/volcano (Fig. 20) forcing produces, in the model, a band with positive anomalies of the 500 hPa height from North America across the central Atlantic to northern Eurasia. The observations show positive anomalies in the geopotential height of the 500hPa layer over the Atlantic region. These anomalies are well simulated for the Atlantic region. The negative anomaly over Greenland was found in all experiments, and also in all observations, with volcanic forcing (isolated and combined with El Niño). Both, in the mod-

elled data and in the observations, a PNA-like pattern is more obvious for mixed forcing then for El Niño forcing alone.

For VOEN, the lower tropospheric temperature (Fig. 21) shows features of the volcanic response in the Eurasian region and features of the El Niño response over North America. The warming in the lower troposphere is strong and shifted somewhat towards the north both in the experiment and in the observations.

The volcano signal can be traced with warming over Scandinavia and in the central part of North America. A large area of negative temperature anomalies in Central Asia is prominent in the mixed case (VOEN) for both, observations and simulations. The positive temperature anomalies over Southeast Asia as well as the warming over the American West Coast are found in the model and in the observations for El Niño winters. The same holds for the cooling over the southeastern USA, while a clear difference between observations and experiments is found over Europe. The observed negative temperature anomalies are not simulated by the model.

7. Summary

We performed an analysis of simulated and observed climate anomalies for El Niño, volcanic, and combined forcing. The results of the simulations and case studies were surveyed in Tab. 7 (Appendix 3). In middle and high latitudes, the atmospheric response to violent volcanic eruptions is modified by a contemporary occurrence of El Niño events. The observed signals of both climate forcing factors are mixed up in middle and high latitudes, because 50 % of the strongest eruptions in the past century are observed together with El Niño periods.

The combination of stratospheric data and near surface temperature records indicates a close correlation between the tropospheric anomalies in the volcanically perturbed winters and in winters with a strong stratospheric polar vortex. Following GRAF et al. (1993a), tropical volcanic stratospheric aerosol forces a natural mode of the stratospheric polar vortex during the northern winter. In periods with high tropical stratospheric aerosol loading, the polar vortex was stronger than otherwise.

Applying a signal detection procedure in the EOF domain, typical signals could be analyzed. In general, El Niño and strong tropical volcanic eruptions lead to regionally different anomalies during winter. With the exception of the observed cold El Niño winters over Europe, the main observed features are also found in the simulations. The commonly local t-test analysis shows different signals for each of the forcing factors. The global significance of the

response is highest for the El Niño signal. The volcanic signal is much weaker. The volcanic signal in the troposphere is embedded in the climate noise. With a multivariate analysis, the signals can be separated much better from climate noise.

The modulation of the planetary wave pattern forces near surface anomalies after violent volcanic eruptions. The effect of local cooling due to the reduction of shortwave radiation over large land areas (like Asia) in subtropical regions, and also the advective warming over Eurasia and the advective cooling over Greenland was simulated in accordance with observations. The amplitude of the volcanic perturbation of the tropospheric geopotential field is larger in the Atlantic region than elsewhere. The radiative cooling near the surface is important in the subtropics, and it is only weak in higher latitudes during winter. In these regions the dynamic response dominates.

The main effect of El Niño forcing occurs in the Pacific region. It is not restricted to the tropics. The well known anomalies in the tropics, the warming over North America in middle and high latitudes are simulated in the same mode as observed. The observed cooling during El Niño over Europe does not occur in the simulations. This difference may be explained with model deficiencies. The stratospheric zonal flow is too strong in the model climate, the variability of the polar vortex is missing, and the perturbation caused by the enhanced Aleutian Low is too small to efficiently disturb the model's polar night jet. The perturbation of the polar vortex by an El Niño (as described in *LABITZKE and van LOON, 1989*) cannot be reproduced without a better representation of the stratosphere in the GCM and higher resolution.

The combination of high stratospheric aerosol loading and El Niño leads to a climate perturbation stronger than for isolated forcings. Over Europe the volcanic signal dominates, and in the Pacific region the El Niño forcing determines the observed and the simulated anomalies in winter. The northern hemisphere analysis separates the volcanic signal better than in the global domain, especially in the lower troposphere, since for the El Niño case the signal is weaker in middle and higher latitudes.

Acknowledgements: We wish express our sincere thanks to Dr. B.Santer for supplying us with the EOF analysis programmes. Thanks are also due to Mrs. J.Perlwitz for preparing the stratospheric data analysis. The authors have benefited from discussions with Drs. B. Santer, H. v. Storch and U. Cubasch. This study was supported by the Bundesministerium für Forschung und Technologie (No. 07 KFT/55A7).

8. Literature

AGU, 1992. *Volcanism and climate change. American Geophysical Union, Special Report, 27pp.*

Asaturov,M.L., M.I. Budyko, K.Ya. Vinnikov, P.Ya. Groisman, A.S. Kabanov, I.L. Karol, M.P. Kolomeev, S.I. Pibobarova, E.V. Rosanov and S.S. Khmelevtsov, 1986. *Vulkani, stratospheri aerozol i klimat zemli (in Russian). Leningrad.*

Bakan, S., 1982. *Strahlungsgetriebene Zellularkonvektion in Schichtwolken. Dissertation, Univ. Hamburg, 99pp.*

Barnett, T.P., M. Latif, E. Kirk and E. Roeckner, 1991. *On ENSO physics. J. Climate, 4, 487-515.*

Berresheim, H. and W. Jaeschke, 1983. *The contribution of volcanoes to the global atmospheric sulfur budget. J. Geophys. Res., 88, 3732-3740.*

Bjerknes, J., 1966. *A possible response of the atmospheric Hadley circulation to equatorial anomalies of ocean temperature. Tellus, 18, 820-829.*

Bluth, G.J.S., S.D. Doiron, A.J. Krueger, L.S.Walter and C.C.Schnetzler, 1992. *Global tracking of the SO_2 clouds from the June, 1991 Mount Pinatubo eruption. Geophys. Res. Lett. 19, 151-154.*

Bradley, R.S., 1988. *The explosive volcanic eruption signal in northern hemisphere continental temperature records. Climate Change, 12, 221-243.*

Cubasch, U., 1985. *The mean response of the ECMWF global model to the El Niño anomaly in extended range prediction experiments. Atmos-Ocean, 23, 43-66.*

Cubasch (ed.), 1991. *First joint climate modelling planning workshop 24th - 25th June 1991. Deutsches Klimarechenzentrum.*

Davis, J.C., 1973. *Statistics and data analysis in Geology. John Wiley, 432-437.*

Dzerdzeevskii, B.L., 1962. *Fluctuations of climate and the general circulation of the atmosphere in extratropical latitudes of the Northern Hemisphere and some problems of dynamic climatology. Tellus, 14, 328-336.*

DKRZ, 1992. *The ECHAM3 atmospheric general circulation model. Technical Report, 6, 184pp.*

Fraedrich, K., K. Müller and R. Kuglin, 1992. *Northern hemispheric circulation regimes during the extremes of the El Niño/Southern Oscillation. Tellus, 44, 33-40.*

Geller, M.A. and J.C. Alpert, 1980. *Planetary wave coupling between the troposphere and the middle atmosphere as a possible sun-weather mechanism. J. Atmos. Sci., 37, 1197-1215.*

Gobbi, G.P., F. Congeduti and A. Adriani, 1992. *Early stratospheric effects of the Pinatubo eruption. Geophys. Res. Letts., 19, 997-1000.*

Graf, H.F., 1986. *Abkühlung der Nordhemisphäre - ein möglicher Trigger für El Niño/Southern Oscillation Episoden. Naturwissenschaften, 73, 258-263.*

Graf, H.F., 1992. *Arctic radiation deficit and climate variability. Climate Dynam., 7, 19-28.*

Graf, H.F., J. Perlwitz and I. Kirchner, 1993a. *Northern hemisphere tropospheric midlatitude circulation after violent volcanic eruptions. MPI Report, 107, 18pp.*

Graf, H.F., I. Kirchner, A. Robock and I. Schult, 1993b. *Pinatubo eruption winter climate effects: Model versus observations. Climate Dynam., (in press).*

Groisman, P.Y., 1992. *Possible regional climate consequences of the Pinatubo eruption: An empirical approach. Geophys. Res. Letts., 19, 1603-1606.*

Hammer, C.U., 1977. *Past volcanism revealed by Greenland ice sheet impurities. Nature, 270, 482-486.*

Hasselmann, K., 1992. *Optimal fingerprints for the detection of time dependent climate change. MPI Report, 88, 41pp.*

Hense, A., 1986. *Multivariate statistical investigations of the northern hemisphere circulation during the El Niño event 1982/83. Tellus, 38, 189-204.*

Hofmann, D.J., 1991. *Aerosols from past and present volcanic emissions. in Aerosols and Climate. V.Hobbs and M.P.McCormick (eds), Deepak Publ., 195-214.*

Horel, J.O. and J.M. Wallace, 1981. *Planetary-scale atmospheric phenomena associated with the Southern Oscillation. Mont. Weath. Rev., 109, 813-829.*

Jones, P.D., S.C.B. Raper, B.S.G. Cherry, C.M. Goodness, T.M.L. Wigley, B. Santer, P.M. Kelly, R.S. Brandley and H.F. Diaz, 1986. *A global grid point surface air temperature data set: 1851-1984.CDIC Numeric Data Collection, NDP-020.*

Kinne, S., O.B. Toon and M.J. Prather, 1992. *Buffering of stratospheric circulation by changing amounts of tropical ozone - a Pinatubo case study. Geophys. Res. Letts., 19, 1927-1930.*

Krueger, A., 1983. *Sighting of El Chichón sulfur dioxide clouds with the Nimbus 7 total ozone mapping spectrometer. Science, 220, 1377-1379.*

Labitzke, K. and B. Naujokat, 1983. *Temperature effects on the stratosphere of the April 4, 1982 eruption of El Chichón, Mexico. Geophys. Res. Letts., 10, 24-26.*

Labitzke, K. and H. van Loon, 1989. *The Southern Oscillation. Part IX: The influence of volcanic eruptions on the Southern Oscillation in the stratosphere. J. of Climate 2, No. 10,1224-1226.*

Labitzke, K., 1992. *Stratospheric temperature data based on radiosonde measurements, (pers. comm.).*

Lacis, A., J. Hansen and M. Sato, 1992. *Climate forcing by stratospheric aerosols. Geophys. Res. Letts., 19, 1607-1610.*

Lamb, H.H., 1977. *Supplementary volcanic dust veil index assessments. Climate Monitor, 6, 57-67.*

Loon, H.v. and K. Labitzke, 1987. *The Southern Oscillation. Part V: The anomalies in the lower stratosphere of the northern hemisphere in winter and a comparison with the Quasi-Biennial Oscillation. Mont.Weath. Rev., 115, 357-369.*

Lough, J.M. and H.C. Fritts, 1987. *An assessment of the possible effects of volcanic eruptions on North American climate using tree-ring data, 1602 to 1900. Climate Change, 10, 219-239.*

Mass, C. F. and D.A. Portman, 1989. *Major volcanic eruptions and climate: A critical evaluation. J. Climate, 2, 566-593.*

Matsuno,T., 1970. *Vertical propagation of stationary waves in the winter northern hemisphere. J. Atmos. Sci., 27, 871-883.*

Namias, J., 1976. *Some statistical and synoptical characteristics associated with El Niño. J. Phys. Oceanogr., 6, 130-138*

Newall, C. G.and S. Self, 1982. *The volcanic explosivity index (VEI): An estimate of explosive magnitude for historical volcanism. J. Geophys. Res., 87, 1231-1238.*

Palmer, T.N., 1988. *Medium and extended range predictability and stability of the Pacific/North American mode. Quart. J. Roy. Meteor. Soc., 114, 691-713.*

Perlwitz, J., 1992. *Untersuchungen des statistischen Zusammenhanges zwischen troposphärischer und stratosphärischer Zirkulation der Nordhemisphäre im Winter mit multivariaten statistischen Analyseverfahren. Diplomarbeit, Humboldt Univ. Berlin, 48pp.*

Perlwitz, J. and H.-F. Graf, 1993. *On the statistical connection between tropospheric and stratospheric circulation of the northern hemisphere in winter. (in preparation).*

Philander, S.G., 1990. *El Niño, La Niña, and the Southern Oscillation. International Geophys.Series, 46, Academic Press, R.Dmowska and J.R.Holton (ed.), 291 pp.*

Pinto, J. P., R.P. Turco and O.B. Toon, 1989. *Self-limiting physical and chemical effects in volcanic eruption clouds. J. Geophys. Res., 94, 11,165-11,174.*

Preisendorfer, R.W., 1988. *Principal component analysis in meteorology and oceanography. Development in Atmos. Sci., 17, Elsevier, Amsterdam, 425 pp.*

Quinn,W.H., D.O. Zopf, K.S. Short and R.T.W. Huo Yang, 1978. *Historical trends and statistics of the Southern Oscillation; El Niño and Indonesian Drought. Fishery Bull., 76, 663-678.*

Rampino, M.R. and S. Self, 1982. *Historic eruptions of Tambora (1815), Krakatau (1883), and Agung (1963), their stratospheric aerosols, and climatic impact. Quaternary Res., 18, 127-143.*

Reiter, R. and H. Jäger, 1986. *Results of 8-year continuous measurements of aerosol profiles in the stratosphere with discussion of the importance of stratospheric aerosols to an estimate of effects on the global climate. Met. and Atmos. Phys., 35, 19-48.*

Robock, A., 1991. *The volcanic contribution to climate change of the past 100 years. in M.E.Schlesinger (ed.), Greenhouse-Gas-Induced Climate Change: A critical appraisal of simulations and observations. Elsevier Sci. Pub. B.V., Amsterdam, 429-443.*

Robock, A. and J. Mao, 1992. *Winter warming from large volcanic eruptions. Geophys. Res. Letts., 19, 2405-2408.*

Roeckner, E., L. Dümenil, E. Kirk, F. Lunkheit, M. Ponater, B. Rockel, R. Sausen and U. Schleese, 1989. *The Hamburg version of the ECMWF model (ECHAM). In Research activities in atmospheric and oceanic modelling. CAS/JSC Working Group on Numerical Experimentation, G.J. Boer (ed.). Report, 13, WMO/TD, 332. 7.1 - 7.4.*

Russell, P.B., R. Pueschel, S. Kinne, E. Dutton, T. Deshler, E. Browell, L. Stowe, M.J. Post, 1993. *Size distribution and optical properties of post-Pinatubo aerosols. Gordon Conference on the Impact of Volcanism on Climate, Henniker, NH, July 26-30, 1993.*

Santer, B.D., W. Brüggemann, U. Cubasch, K. Hasselmann, H. Höck, E. Maier-Reimer, U. Mikolajewicz, 1993. *Signal-to-noise analysis of time-dependent greenhouse warming experiments. Part 1: Pattern analysis. Climate Dynam., (submitted).*

Simkin,T., L. Siebert, L. McClelland, D. Bridge, C.G. Newhall and J.H. Latter, 1981. *Volcanoes of the World. Hutchinson Ross, Stroudsburg, PA, 240 pp.*

Schmitz, G. and N. Grieger, 1980. *Model calculations of the structure of planetary waves in the upper troposphere and lower stratosphere as a function of the wind field in the upper stratosphere. Tellus, 32, 207-214*

Schult, I., 1991. *Bildung und Transport von Aerosolteilchen in der Stratosphäre und ihre Bedeutung für den Strahlungshaushalt. Examensarbeit, 11, MPI, 142pp.*

Sear, C.B, P.M. Kelly, P.D. Jones and C.M. Goodess, 1987. *Global surface-temperature response to major volcanic eruptions. Nature, 330, 365-367.*

Shukla, J. and Fennessy, M.J., 1988. *Prediction of time mean atmospheric circulation and rainfall influence of pacific SST anomaly. J. Atmos. Sci., 45, 9-40.*

Simkin,T., L. Siebert, L. McClelland, D. Bridge, C.G. Newhall, J.H. Latter, 1981. *Volcanoes of the world. Hutchinson Ross, Stroudsburg, PA, 240 pp.*

Spencer, R.W. and J.R. Christy, 1991. *Global temperature update to 31 October 1991. NASA Headquarters, Washigton, (pers. comm.).*

Spirina, L.P., 1973. *On the seasonal changes of the surface air temperature field of the Northern Hemisphere after volcanic eruptions (in Russian), Trans. of the Main Geophysical Observatory, 299, 3-7.*

Spiro, P.A., D.J. Jacob, J.A. Logan, 1992. *Global inventory of sulfur emmission with 1°x1° resolution. J. Geophys. Res., 97, 6023-6036.*

Storch,H.v. and H.A. Kruse, 1985. *The extra-tropical atmospheric response to El Niño events - a multivariate significance analysis. Tellus, 37, 361-377.*

Storch, H.v. and F.W. Zwiers, 1988. *Recurrence analysis of climate sensitivity experiments. J. Climate, 1, 157-171.*

Taubenheim, J., 1974. *Zur Berücksichtigung der Autokorrelation bei statistischen Tests von Durchschnitten, Streuungen und überlagerten Stichtagen. Gerlands Beitr. Geophys., 3, 121-128.*

Turco, R.P., O.B. Toon, R.C. Whitten, P. Hamill and R.G. Keesee, 1983. *The 1980 eruption of Mount St. Helens: Physical and chemical processes in the stratospheric clouds. J. Geophys. Res., 88, 5299-5319.*

Wendler, G., 1984. *Effects of the El Chichón volcanic cloud on solar radiation received at Fairbanks, Alaska. Bull. Americ. Met. Soc., 65, 216-218.*

Wright, P.B., 1991. *Homogenised sea surface temperature from the COADS and sea surface temperature from Climate Diagnostic Bulletin of the Climate Analysis Centre.*

A 1. Strong volcano events since 1850

Table 1. *Volcano eruptions (VEI ≥4 and/or DVI ≥ 200):*

Location	Eruption date	Volcano	VEI (DVI)
43°N, 141°E	Apr/1853	Usudake (Japan)	4
50°N, 155°E	Dec/1853	Chikurachki(Kuriles Island)	4
57°N, 162°E	Feb/1854	Sheveluch (Kamchatka)	5
1°S, 78°W	Nov/1855	Cotopaxi(Ecuador)	2(700)
42°N, 141°E	Sep/1856	Komatagake (Hokkaido)	4
1°N, 127°E	Dec/1861	Makian (Spice Islands)	4(800)
2°N, 76°W	Oct/1869	Purace (Colombia)	4
49°N, 154°E	Apr/1872	Sinarka (Kuriles)	4
64°N, 17°W	Jan/1873	Grimsvøtn (Iceland)	4
65°N, 17°W	Mar/1875	Askja (Iceland)	5(1000)
30°N, 130°E	Apr/1877	Suwanose-Jima (Oshima)	4
1°S, 78°W	Jun/1877	Cotopaxi (Ecuador)	4
6°S, 105°E	Aug/1883	Krakatoa (Sumatra)	6(1000)
59°N, 153°W	Oct/1883	Augustine (Aleutians)	4
1°S, 78°W	Jan/1886	Tungurahua (Ecuador)	4
38°S, 177°E	Jun/1886	Tarawera (New Zealand)	5(800)
38°N, 140°E	Jul/1888	Bandai (Hondo)	4(500)
30°N, 130°E	Oct/1889	Suwanose-Jima (Oshima)	4
2°N, 80°W	Nov/1899	Donna Juana (Columbia)	4
15°N, 61°W	May/1902	Mt.Pelee (Antilles)	4
13°N, 61°W	May/1902	Soufriere (Antilles)	4(300)
15°N, 92°W	Oct/1902	St.Maria (Guatemala)	6(600)
52°N, 158°E	Mar/1907	Ksudach (Kamchatka)	5(500)
43°N, 141°E	Mar/1909	Tarumai (Hokkaido)	4
14°N, 121°E	Jan/1911	Taal (Philippine Islands)	4
58°N, 155°W	Jun/1912	Katmai (Alaska)	6(500)
32°N, 131°E	Jan/1914	Sakura-Jima (Oshima)	4
19°N, 146°E	Apr/1917	Agrigan (Marian Islands)	4
1°S, 78°W	Apr/1918	Tungurahua (Ecuador)	4
64°N, 19°W	Oct/1918	Katla (Iceland)	4
4°S, 145°E	Aug/1919	Manam (New Guinea)	4
41°S, 72°W	Dec/1921	Puyehue (Chile)	4(200)
48°N, 153°E	Feb/1924	Raikoke (Kuriles)	4
42°N, 141°E	Jun/1929	Komaga-Take (Hokkaido)	4
56°N, 161°E	Mar/1931	Kliushevskoi (Kamchatka)	4
14°N, 91°W	Jan/1932	Fuego (Guatemala)	4
36°S, 71°W	Mar/1932	Quizapu/Cerro Azul (Chile)	5
4°S, 152°E	May/1937	Rabaul (New Britain)	4
56°N, 161°E	Jan/1945	Kliushevskoi (Kamchatka)	4
48°N, 153°E	Nov/1946	Sarychev Peak (Kuriles)	4
64°N, 20°W	Mar/1947	Hekla (Iceland)	4
16°S, 168°E	Dec/1950	Ambrym (New Hebrides)	4
9°S, 148°E	Jan/1951	Lamington (Papua)	4
6°S, 155°E	Feb/1952	Bagana (Salomon Islands)	4
61°N, 152°W	Jul/1953	Mt.Spurr (Aleutians)	4
40°S, 72°W	Jul/1955	Nilahue (Chile)	4
56°N, 161°E	Mar/1956	Bezymianny (Kamchatka)	5
8°S, 116°E	Mar/1963	Agung (Java)	4(800)
57°N, 162°E	Nov/1964	Sheveluch (Kamchatka)	4
14°N, 121°E	Sep/1965	Taal (Philippine Islands)	4
8°S, 122°E	Apr/1966	Kelut (Java)	4
4°N, 126°E	Aug/1966	Awu (Sangihe Island)	4(200)
3°S, 36°W	Aug/1966	Olynoyo Lengai (Kenia)	4
EQ, 92°W	Jun/1968	Fernandia (Galapagos Islands)	4
44°N, 146°E	Jul/1973	Tiatia (Hokkaido)	4
14°N, 91°W	Oct/1974	Fuego (Guatamala)	4(250)
56°N, 160°E	Jul/1975	Plosky Tolbachik (Kamchatka)	4
59°N, 153°W	Jan/1976	Augustine (Aleutians)	4
56°N, 161°E	Feb/1979	Bezymianny (Kamchatka)	4
46°N, 122°W	May/1980	St.Helens (USA)	5(500)
51°N, 155°E	Apr/1981	Alaid (Kuriles)	4
18°N, 146°E	May/1981	Pagan (Mariana Island)	4
1°S, 29°E	Dec/1981	Nyamuragira (Zaire)	4
4°N, 93°W	Apr/1982	El Chichon (Mexico)	5(800)
7°S, 108°E	May/1982	Galunggung (Java)	4
EQ, 122°E	Jul/1983	Una Una (Celebes)	4
5°N, 75°W	Nov/1985	Nevado del Ruiz (Columbia)	4
59°N, 153°W	Apr/1986	Augustine (Aleutians)	4
55°N, 162°W	Apr/1986	Pavloff (Aleutians)	4
8°S, 112°E	Feb/1990	Kelut (Java)	4
14°N, 73°W	Jun/1991	Pinatubo (Philippine Islands)	5
46°S, 73°W	Aug/1991	Cerro Hudson (Chile)	5

A 2. Signal selection methods

A 2.1. Local t-test

We defined the average anomaly according to (1), with X being any meteorological parameter (temperature, zonal wind, etc.) and X beeing its average over time. Subscript e indicates the experiment and c indicates the control run.

$$(1) \qquad X'_e(x,y) = \overline{X}_e(x,y) - \overline{X}_c(x,y)$$

The amplitude of the anomaly of any meteorological parameter X' was tested with the local t-test (equations 2 and 3). The value $n_{e/c}$ is the number of months used, and $S_{e/c}$ is the dispersion of the control and experiment data, respectively. $S_{e,c}$ indicates the weighted dispersion.

$$(2) \qquad t_e(x,y) = \frac{X'_e(x,y)}{S_{e,c}}$$

$$(3) \qquad S^2_{e,c} = \frac{\{(n_e-1)S^2_e + (n_c-1)S^2_c\}}{n_e+n_c-2}$$

The value of t_e describes the statistical significance of any parameter X on the spatial point (x,y). The number of degrees of freedom depends on the number of independent months. We estimated this number from the autocorrelation function $a_x(x,y;t)$. The expression in brackets of (4) is the so-called "Bartels'sche Erhaltenszahl" (Bartels [1936], see in *TAUBENHEIM, 1974*).

$$(4) \qquad N_{eff;X_{e,c}}(x,y) = n_{e,c}\left[1 + \sum_{\tau=1}^{n_{e,c}-1} \frac{(n_{e,c}-\tau)}{n_{e,c}} \alpha_X(x,y;\tau)\right]^{-1}$$

A 2.2. Signal-to-noise analysis

Anomalies were computed for the experiment data according to (5), and for the reference data according to (6).

$$(5) \qquad x'_e(x,y;t) = x_e(x,y;t) - \overline{X}_c(x,y)$$

$$(6) \qquad x'_c(x,y;t) = x_c(x,y;t) - \overline{X}_c(x,y)$$

Both anomaly data sets x'_e and x'_c were represented by two orthonormal bases, EOF_e and EOF_c, with the spatial dimension of x multiplied with y. The number of basis vectors is n_{eof} (see equation [7]).

$$(7) \qquad n_{eof} = min\,[\,(x \cdot y), t-1\,]$$

The first set of basis vectors EOF_e was estimated from the experiment anomaly data set x'_e, and the second set EOF_c is based on the reference anomaly data x'_c. For each set we computed an ensemble of Principal Component (PC) time series (equation [8]). n indicates the position of the PC time series in the set. It varies for each set between *1* and n_{eof}.

$$(8) \qquad PC^{\nu}_{e,c;EOF_{e,c}}(t) = \sum_{\xi=1}^{x}\sum_{\eta=1}^{y} x'_{e,c}(\xi,\eta;t)\cdot EOF^{\nu}_{e,c}(\xi,\eta)$$

With these PCs we can compute the ratios of the variance (equation [9]) of each subset of EOFs in the experiment and control data sets. The value n_n indicates different subsets of the basic EOF set. The number of EOFs explaining 95% of total variance in the reference data set is one possible number for n_n.

$$(9) \qquad V^{n_\nu}_{e,c;EOF_{e,c}} = \frac{\left(\sum_{\nu=1}^{n_\nu}\sum_{\tau=1}^{t}\left(PC^{\nu}_{e,c;EOF_{e,c}}(\tau)\right)^2\right)}{\left(\sum_{\xi=1}^{x}\sum_{\eta=1}^{y}\sum_{\tau=1}^{t}(x'_{e,c}(\xi,\eta;\tau))^2\right)}$$

Another rule for n_n is based on Monte Carlo simulations (*PREISENDORFER, 1988*). Ensembles of random data sets (m = number of different random data sets) with the same temporal and spatial dimensions as those at which the experiment and reference data were analyzed. In a diagram of explained variance over EOF number, for each EOF a distribution of the explained variance can be drawn. On the upper side of this distribution we can cut for each EOF number the m_b ($m_b = m*b/100$ %) elements with the largest explained variance. Then the line connecting those points is the threshold for a meaningful EOF with the estimation error of b (in our case b = *5* %) comparable with a white noise process. Only EOFs with variance higher than this range give more information than white noise. This number of EOFs with information is smaller than the number of EOFs describing 95 % of total variance. The cumulative variance explained by this "informative" EOFs defines the objective information

potential. This information potential is limited by the spatial and temporal dimensions. The estimation of the *EOF*s is accurate only for n_{eof} following equation (7).

The absolute values of n_n are measures of the spatial-temporal coherence and amplitude of signal and climate noise. A small number of n_n for experiment data, and a high number of n_n for control data are associated with low-dimensional response signals embedded in a much higher-dimensional climate space. On the other hand, the ratios of variance following (9) are measures for the signal-to-noise ratio (*SANTER et al., 1993*). The ratio is near 1 for lacking orthogonality between experiment signal and climate noise, and it is near zero for orthogonal patterns.

A 2.3. Signal amplitude analysis

Because of equation (6), the time average for $PC_{c;EOFe}$ is zero for all numbers of *EOF*s. The time average of experiment $PC_{e,EOFe}$ also measures the average signal amplitude of the corresponding spatial pattern. In first order we performed the t-test to analyze the statistical significance of the difference between the experiment run *PC* time average and the control run *PC* time average (in our case zero) for each *EOF*. In our computation this PC^t_e is statistically significant with a probability of more than 99 % for a t-test value greater than 2.75. This estimation yet is not sufficient for the average amplitude.

A second test of the difference between the experiment signal and the climate noise based on a Monte Carlo statistics was performed. For this test, the anomaly data of the experiment and of the control run were mixed. A mixed data set was performed from 50 % of experiment data and 50 % of control data. This random subset was then projected onto the experiment *EOF* vectors. The original experiment data projections are compared with the random subset average amplitude using Student's t-test. This procedure was performed for fifty different random subsets. The relative number of differences between random average and experiment average, exceeding the sigificance level, is a measure of the strength of the signal.

The average signal P_e can be calculated as an overlay of patterns weighted with the mean amplitude of the corresponding principal component for any significant *PC* following equation (10).

$$\overline{P}_e(x,y) = \left[\overline{PC_e}^t EOF_e(x,y)\right]_{n_1} + \left[\overline{PC_e}^t EOF_e(x,y)\right]_{n_2} + \ldots \qquad (10)$$

The value $P_e(x,y)$ represents the average response of the model to the prescribed forcing and n_i corresponds to the *EOF*-position in the EOF_e set for significant amplitudes.

A 3. Signal selection results of the perpetual January experiments

Table 2. *Estimation of the signal-to-noise ratio for volcano, volcano/El Niño and El Niño experiments*

	Volcano (VOLC)		Volcano/El Niño (VOEN)		El Niño (EN)	
Reference EOF	EOF_c	EOF_c	EOF_c	EOF_c	EOF_c	EOF_c
Near surface air temperature						
n_{MC} 1)	16	16	14	16	15	16
V^{nMC}_{ref} 2)	84%	84%	83%	84%	84%	84%
V^{nMC} 3)	64%	59%	61%	54%	63%	50%
V^{nMC} / V^{nMC}_{ref} 4)	0.76	0.70	0.73	0.64	0.75	0.60
Temperature 850hPa						
n_{MC}	20	18	18	18	16	18
V^{nMC}_{ref}	83%	81%	82%	81%	80%	81%
V^{nMC}	55%	53%	54%	46%	52%	43%
V^{nMC} / V^{nMC}_{ref}	0.66	0.65	0.66	0.57	0.65	0.53
Geopotential height 500hPa						
n_{MC}	17	18	15	18	16	18
V^{nMC}_{ref}	87%	88%	86%	88%	87%	88%
V^{nMC}	67%	70%	65%	63%	66%	61%
V^{nMC} / V^{nMC}_{ref}	0.77	0.80	0.76	0.72	0.76	0.69
Zonal wind 200hPa						
n_{MC}	22	24	13	24	14	24
V^{nMC}_{ref}	85%	85%	83%	85%	82%	85%
V^{nMC}	53%	56%	40%	52%	43%	49%
V^{nMC} / V^{nMC}_{ref}	0.62	0.66	0.48	0.61	0.52	0.58
Temperature 50hPa						
n_{MC}	4	10	4	10	10	10
V^{nMC}_{ref}	96%	87%	94%	87%	87%	87%
V^{nMC}	62%	60%	62%	55%	77%	75%
V^{nMC} / V^{nMC}_{ref}	0.65	0.69	0.66	0.63	0.89	0.86
Zonal wind 50hPa						
n_{MC}	12	13	11	13	12	13
V^{nMC}_{ref}	89%	88%	87%	88%	88%	88%
V^{nMC}	74%	76%	72%	76%	73%	74%
V^{nMC} / V^{nMC}_{ref}	0.83	0.86	0.83	0.86	0.83	0.84

1) the number of EOFs explained more of the total spatial-temporal variance as white noise in the reference data set
2) the explained total spatial-temporal variance of reference EOFs (information potential) in the reference data set
3) the explained total spatial-temporal variance of reference EOFs (information potential) in the corresponding data set
4) the ratio of signal-to-noise

Table 3. EOF results of global signal selection for the volcano experiment (the first column contains the rank of the selected EOF, the second column contains the explained variance of the EOF, the third column contains the time-averaged principal component, the last tree columns contain the Monte Carlo amplitude test for tree different significance levels)

Parameter	Volcano (VOLC)					
	n	$V^n_{e;EOFe}$	$\overline{PC_e}^t$	Relative number of mixed sets exceeding the significane level (SL) of the amplitude test		
				SL = 99%	SL = 95%	SL = 90%
T 2m (Celsius)	1 3 4	19% 9% 8%	16.2 7.86 8.64	18% 0% 0%	62% 20% 20%	70% 30% 42%
T 850 hPa (Celsius)	1	17%	17.4	92%	100%	100%
Z 500 hPa (gpm)	1	19%	457	68%	100%	100%
U 200 hPa (m/s)	1	20%	68.4	100%	100%	100%
T 50 hPa (Celsius)	1	88%	181	100%	100%	100%
U 50 hPa (m/s)	1	29%	75.5	100%	100%	100%

Table 4. EOF results of global signal selection for the combined experiment (columns see Table 3)

Parameter	Volcano/El Niño (VOEN)					
	n	$V^n_{e;EOFe}$	$\overline{PC_e}^t$	Relative number of mixed sets exceeding the significane level (SL) of the amplitude test		
				SL = 99%	SL = 95%	SL = 90%
T 2m (Celsius)	1	28%	29.1	100%	100%	100%
T 850 hPa (Celsius)	1	29%	28.9	100%	100%	100%
Z 500 hPa (gpm)	1	31%	757	100%	100%	100%
U 200 hPa (m/s)	1	53%	163	100%	100%	100%
T 50 hPa (Celsius)	1	83%	168	100%	100%	100%
U 50 hPa (m/s)	1 2	38% 17%	38% 17%	67% 0%	98% 4%	100% 33%

Table 5. *EOF results of global signal selection for the El Niño experiment (columns see Table 3)*

Parameter	El Niño (EN)					
	n	$V^n_{c;EOFc}$	$\overline{PC_c}^t$	Rrelative number of mixed sets exceeding the significane level (SL) of the amplitude test		
				SL = 99%	SL = 95%	SL = 90%
T 2m (Celsius)	1	26%	30.1	100%	100%	100%
T 850 hPa (Celsius)	1	28%	29.0	100%	100%	100%
Z 500 hPa (gpm)	1	26%	648	100%	100%	100%
U 200 hPa (m/s)	1	47%	139	100%	100%	100%
T 50 hPa (Celsius)	1 4	30% 6%	18.8 13.6	0% 22%	2% 76%	10% 88%
U 50 hPa (m/s)	1 3	31% 10%	56.8 30.0	26% 6%	68% 70%	88% 88%

Table 6. *The explained variance of the signal following the global and the northern hemispheric (30°N - 80°N) analysis, the values in brackets are the numbers of significant EOFs*

Parameter	Global analysis			Analysis for 30°N - 80°N		
	Volcano (VOLC)	Volcano/El Niño (VOEN)	El Niño (EN)	Volcano (VOLC)	Volcano/El Niño (VOEN)	El Niño (EN)
T 2m	37%(3)	28%(1)	26%(1)	51%(4)	26%(2)	21%(5)
T 850 hPa	30%(3)	29%(1)	28%(1)	47%(4)	33%(2)	39%(2)
Z 500 hPa	36%(2)	31%(1)	26%(1)	22%(1)	24%(1)	46%(2)
U 200 hPa	20%(1)	53%(1)	47% (1)	33% (1)	44%(3)	27%(1)
T 50 hPa	88%(1)	83%(1)	56%(3)	62%(2)	65%(2)	3%(2)
U 50 hPa	29%(1)	55%(2)	41%(2)	38%(1)	72%(3)	40%(2)

Table 7. The atmospheric response to volcanic aerosols and El Niño type sea surface temperature anomalies during winter

	Volcano	Volcano/El Niño	El Niño
Mid- and higher latitudes			
Stratosphere	stronger cyclonic polar vortex than normal		weak polar vortex
	cooling	weaker cooling than in the volcano case centered over Spitsbergen	warming in the North Pacific region, cooling in Scandinavia
Troposphere	strengthened polar night jet stream in the North Atlantic region	weak west wind anomalies over North America and the northern Atlantic	strengthened subtropical jet stream in the North Pacific region
	Greenland strong cooling, Eurasia strong warming	Greenland cooling, Eurasia and northwestern America warming, cooling in the central part of Asia	westcoast of North America warm
Tropics and subtropics			
Stratosphere	no significant signal in the wind field	northward of the equator negative anomalies of the zonal wind field, southward of the equator positive anomalies	
	warming		cooling
Troposphere	no significant signal	westerly wind anomalies in the Pacific region, easterly anomalies over the Atlantic, Africa and the Indian ocean	
	northern Africa and India moderate cooling	positive anomalies of the temperature centred over the East Pacific	

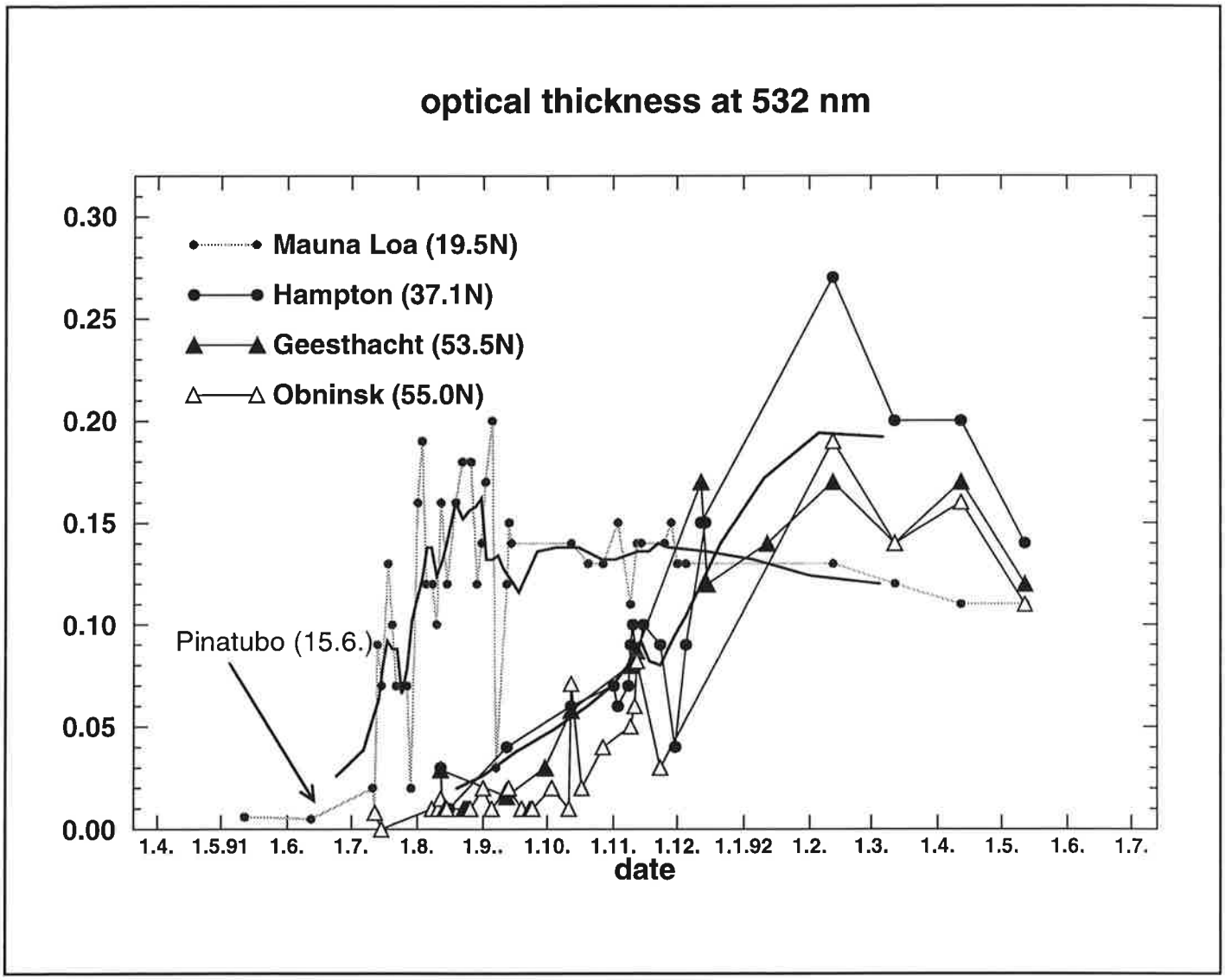

Figure 1. *The optical thickness (normalized to a wavelength at 532 nm) after the Mount Pinatubo eruption in June 1991 based on Lidar observations for stations on different latitudes bands (dark lines are smoothed curves for the stations Mauna Loa and Hampton)*

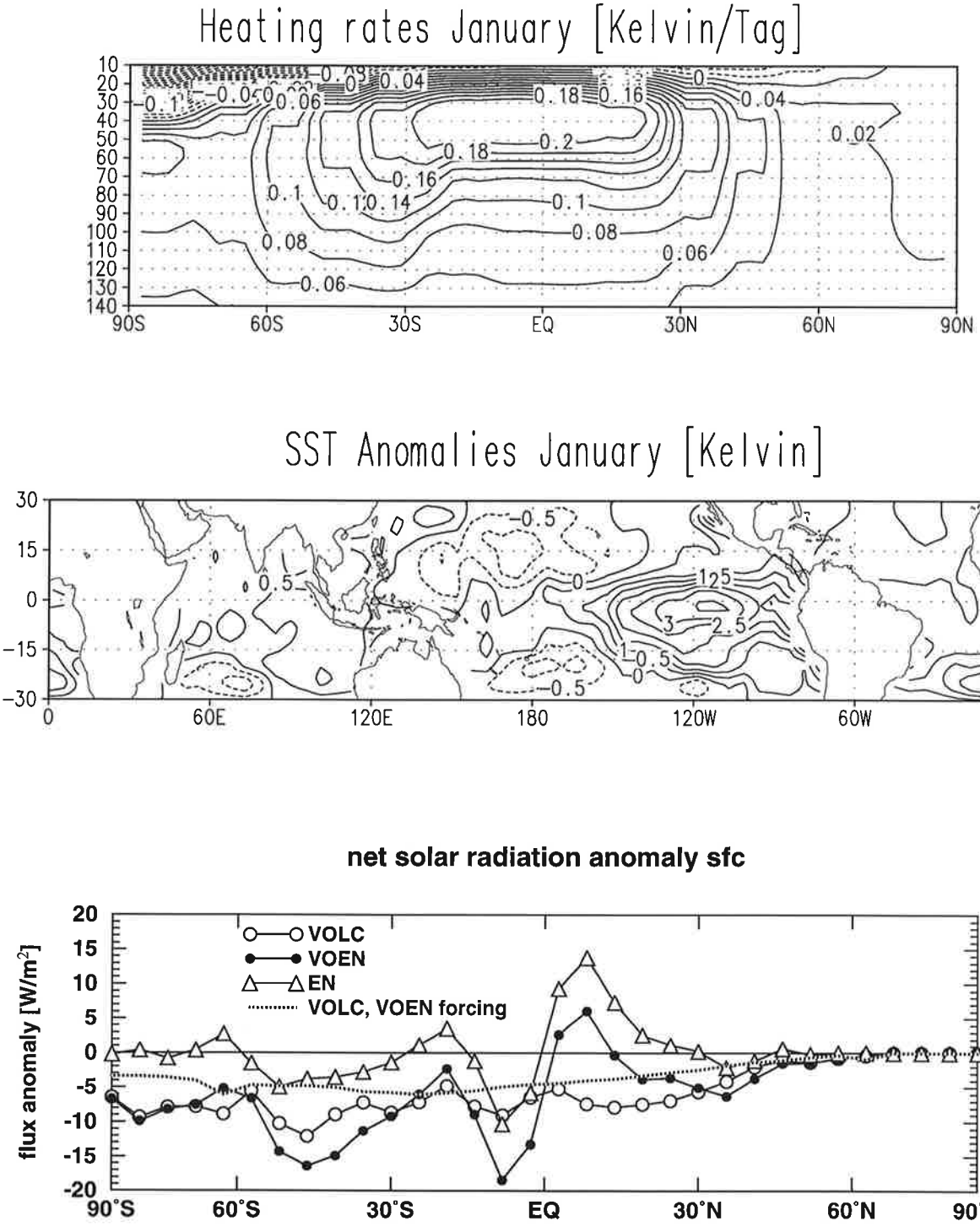

Figure 2. *The volcano experiment heating rates in the stratosphere (upper panel), the El Niño case SST anomaly forcing (middle panel) and the surface solar net fluxes for three forcing experiments (lower panel; in the volcano experiments the external solar flux reduction is one part of these anomalies)*

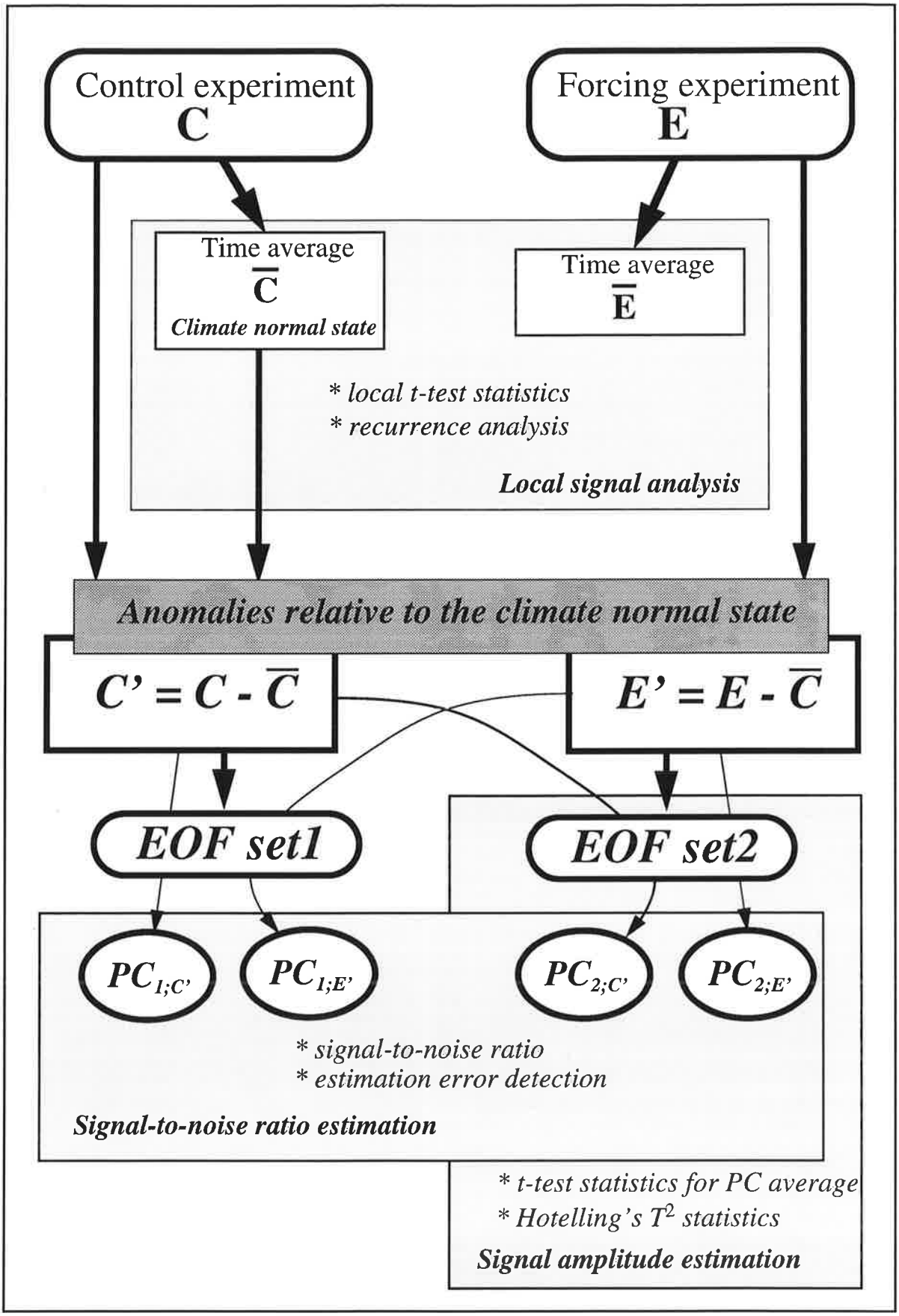

Figure 3. *Schema of the signal selection method*

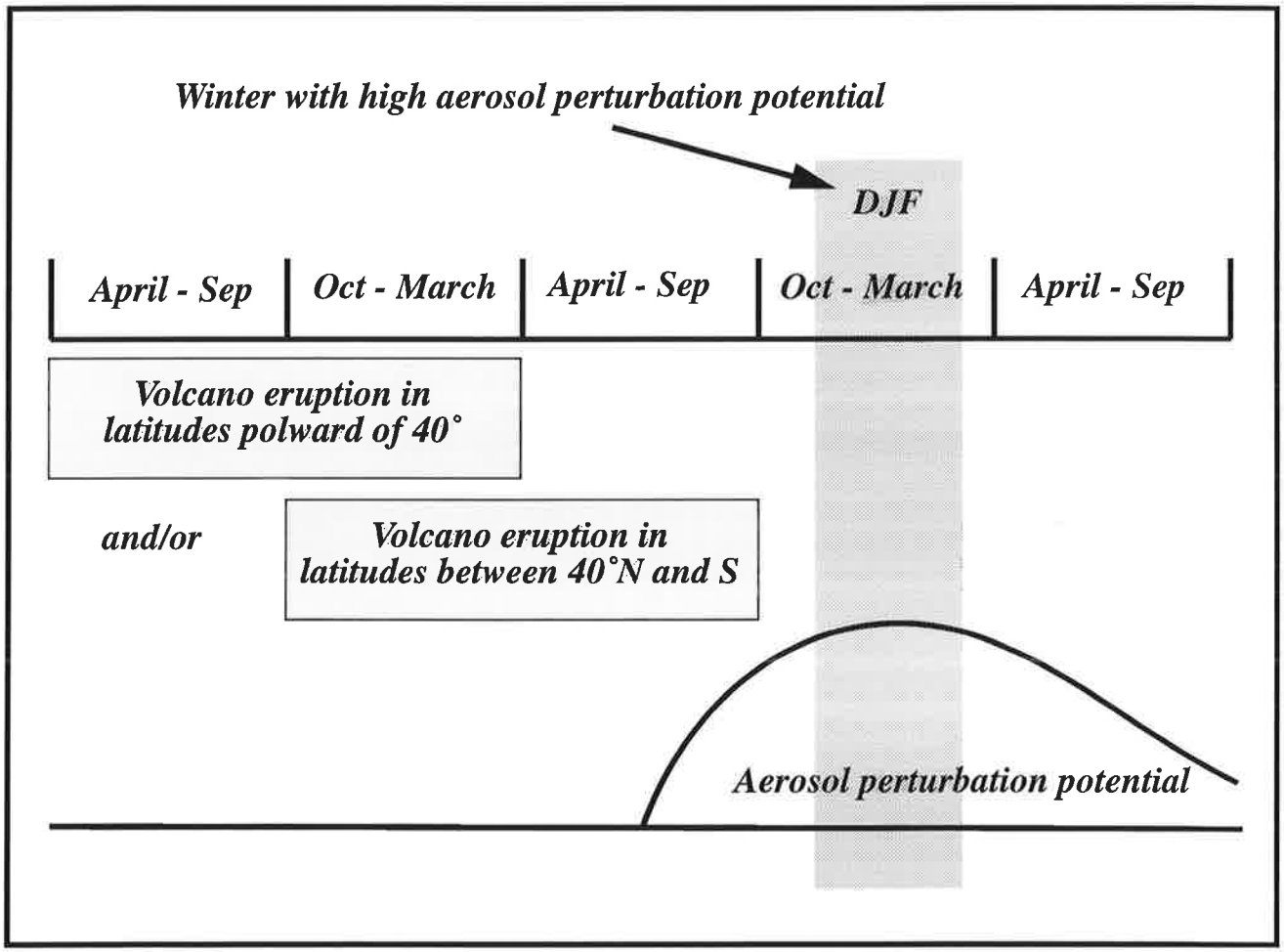

Figure 4. *The definition of volcano-influenced winters as a function of the latitude of the volcano and the eruption date*

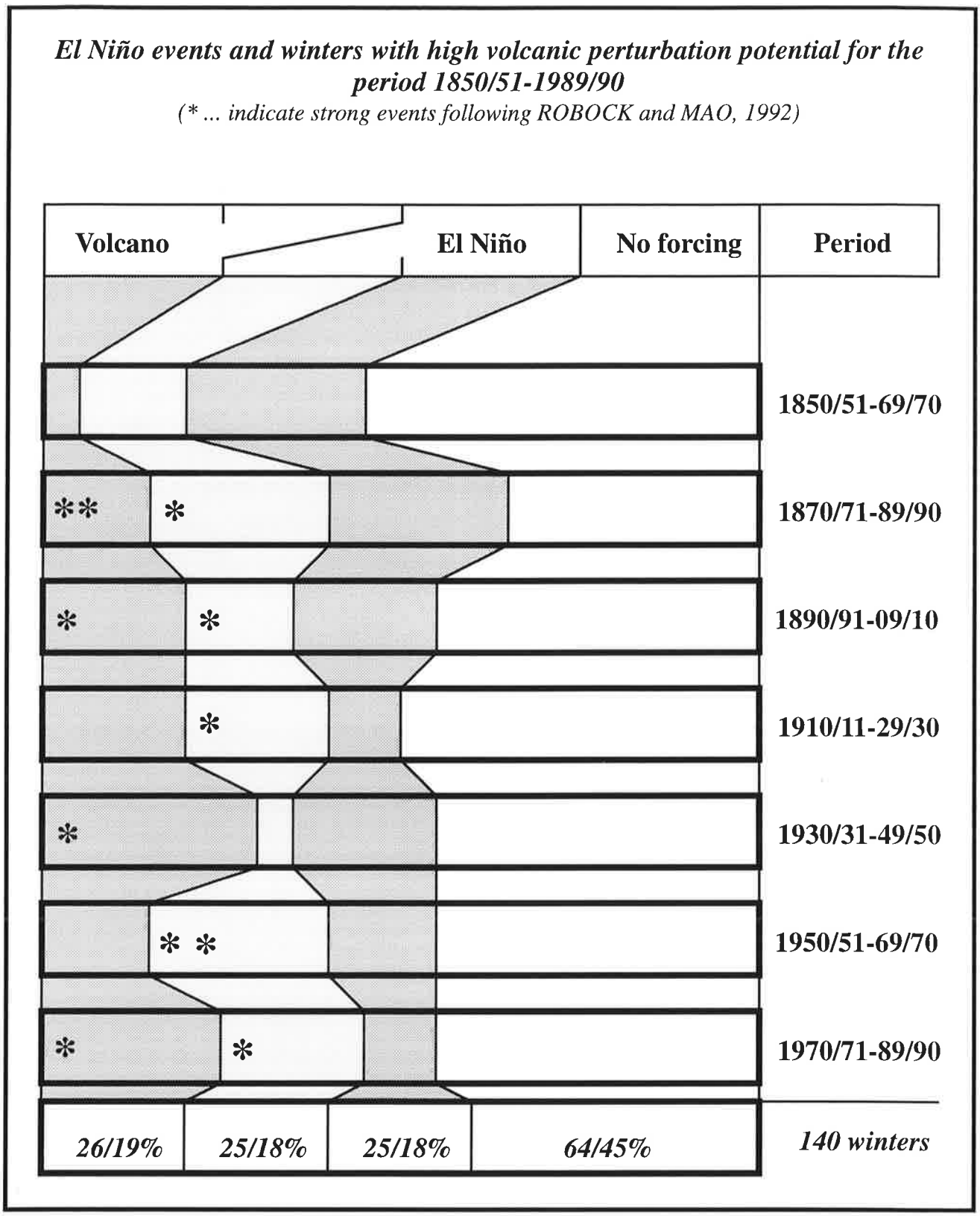

Figure 5. *The number of winters with high volcanic perturbation potential, with volcanic and El Niño forcing, with El Niño, and the residual part of each twenty-year period between 1850 and 1990 (dark grey shaded columns indicate the part with single forcing winters, the light grey shaded column indicates the part with both forcing factors, stars indicate eruptions with VEI >4, the last row contains the absolute number of winters in each class and the part relative to all winters)*

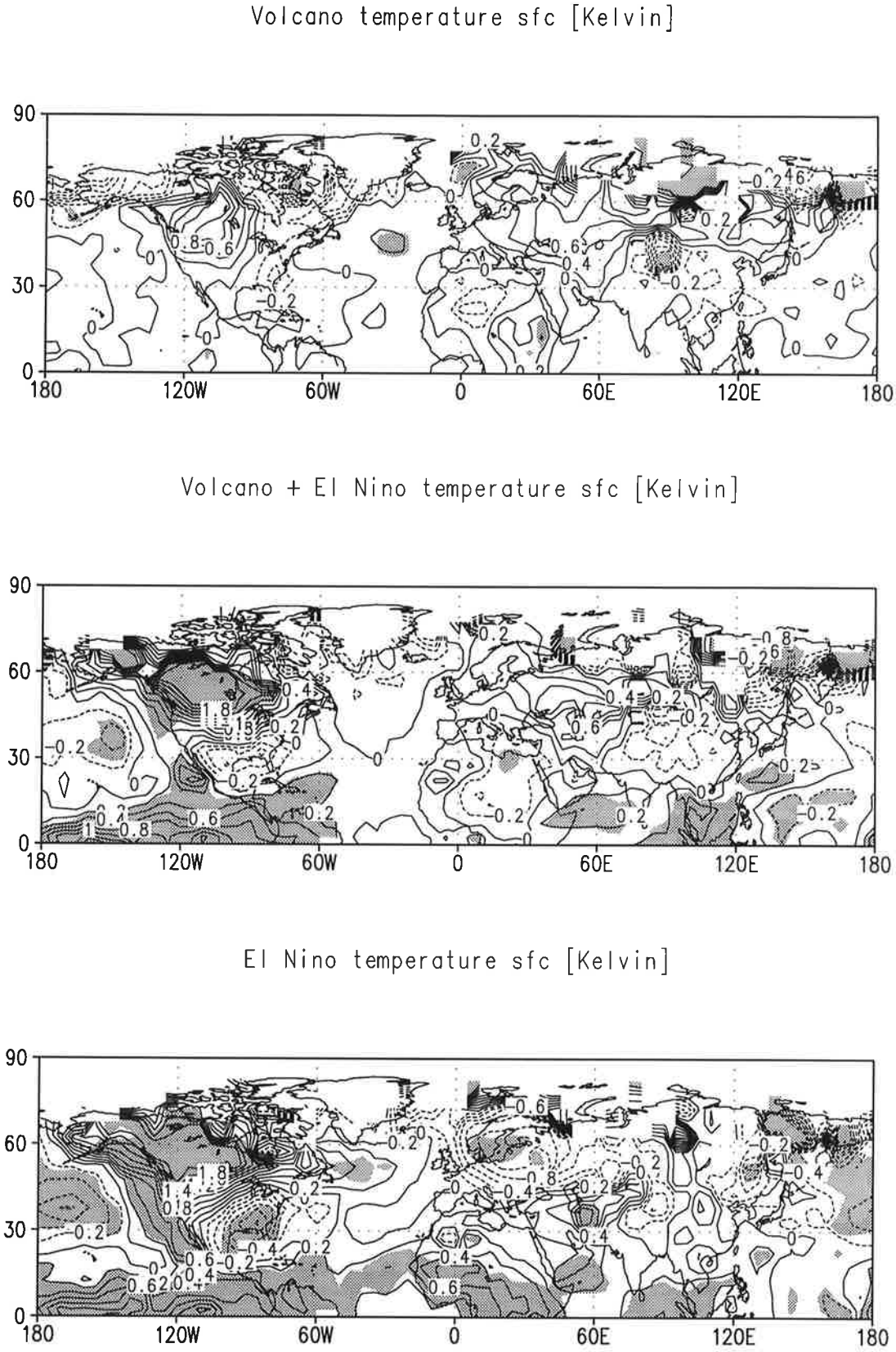

Figure 6. *Surface air temperature anomalies for volcano, El Niño and volcano / El Niño influenced winters in relation to unperturbed winters following observations for the period 1854 to 1992 (JONES et al., 1986, update 1992), shaded areas indicate regions with significance level higher than 99%*

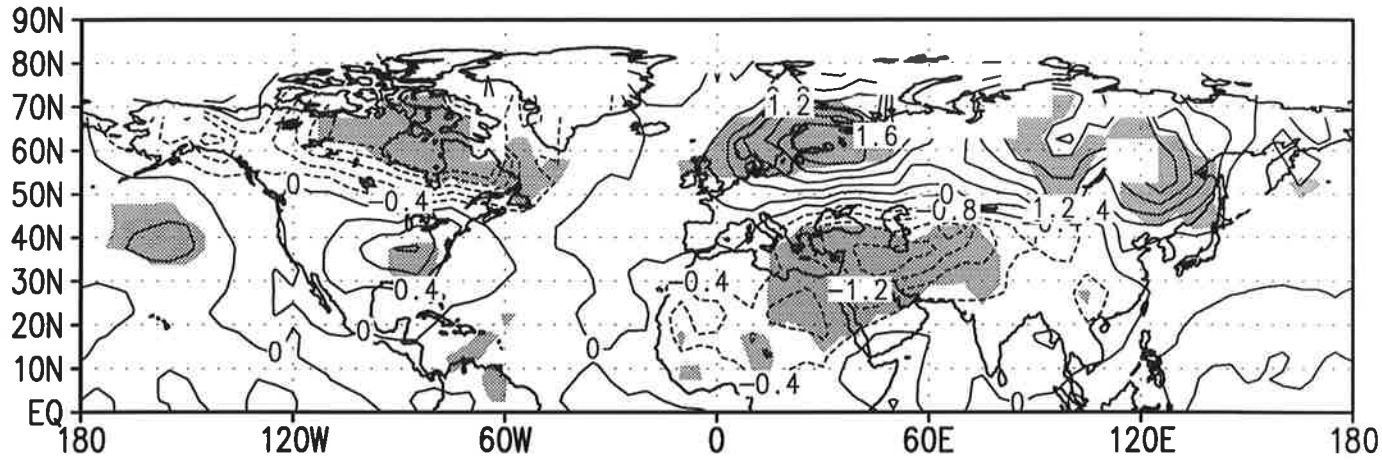

Figure 7. *Surface air temperature anomalies for winter months with strong and weak polar vortexes in relation to unperturbed months for the period 1957 to 1992 (temperature data based on JONES et al., 1986, update 1992; stratospheric vortex observations based on geopotential heights of the 50 hPa level after LABITZKE, 1992), shaded areas indicate regions of anomalies with significance level higher than 99%)*

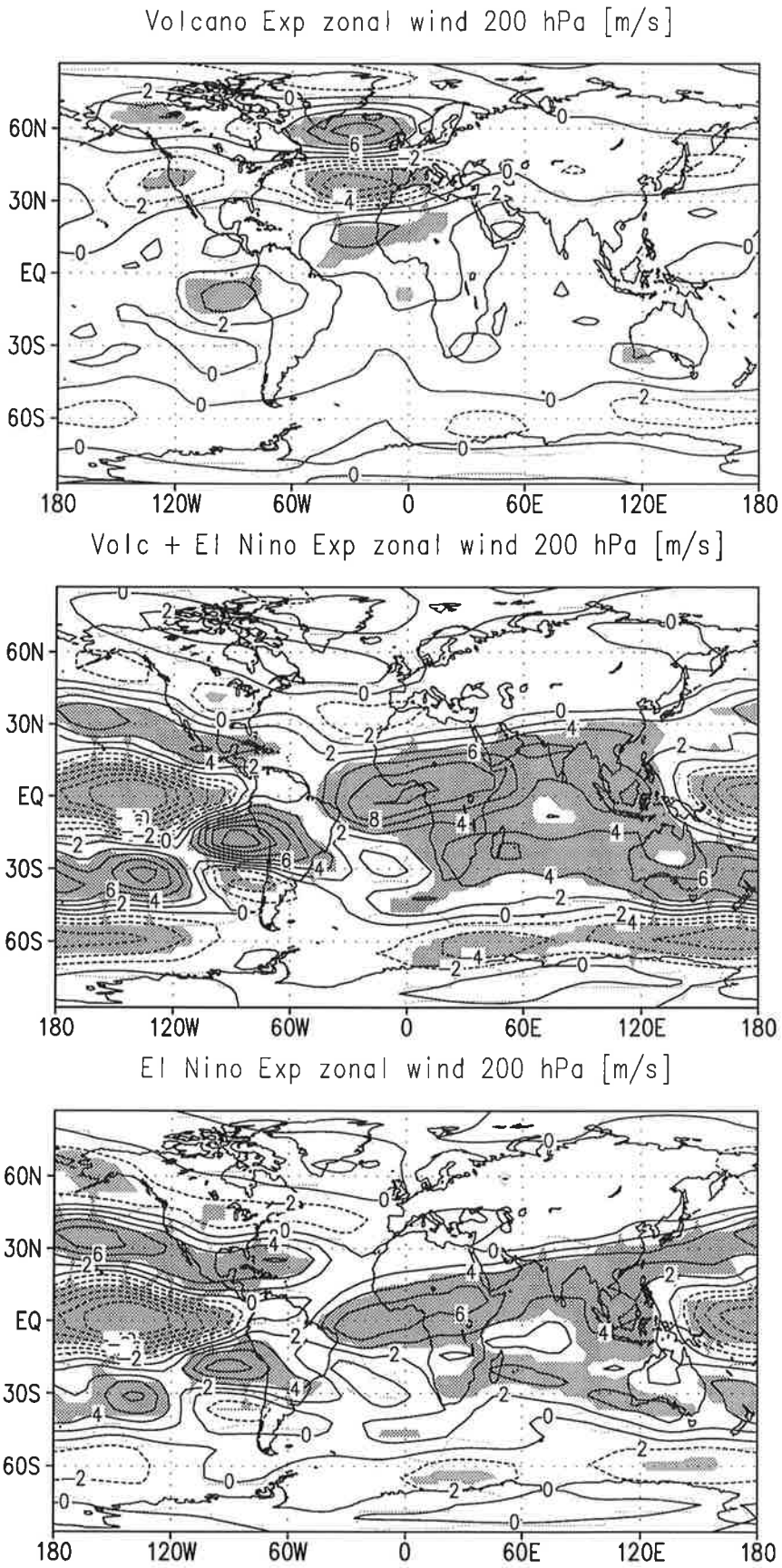

Figure 8. *The zonal wind anomalies in the 200 hPa level for the volcano experiment (upper panel), the combined experiment (middle panel) and the El Niño experiment (areas with significance level higher than 99% are shaded)*

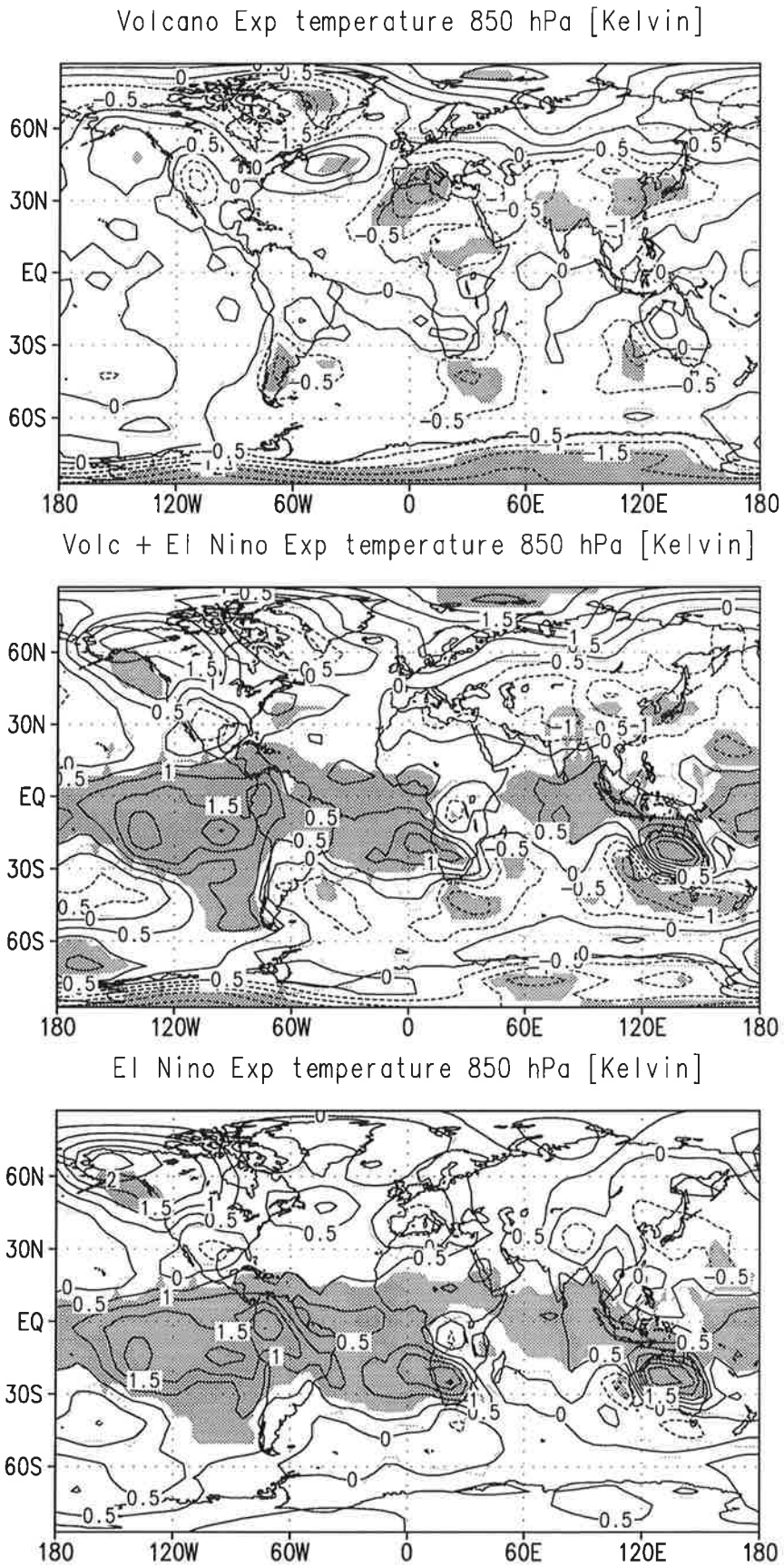

Figure 9. *The temperature anomalies in the 850 hPa level (panels see Fig. 8)*

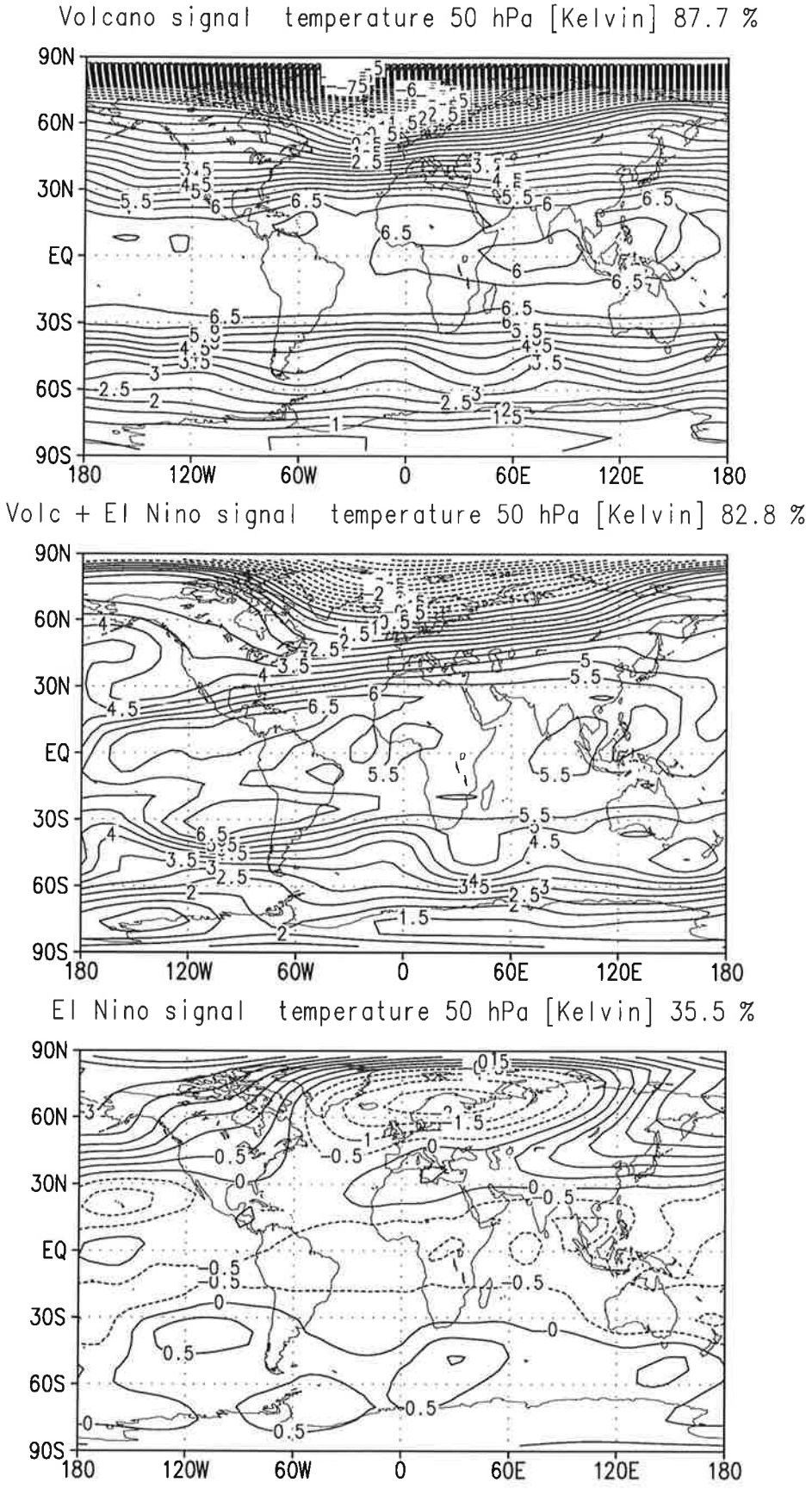

Figure 10. *The EOF filtered signal of the temperature in the 50 hPa level (panels see Fig. 8)*

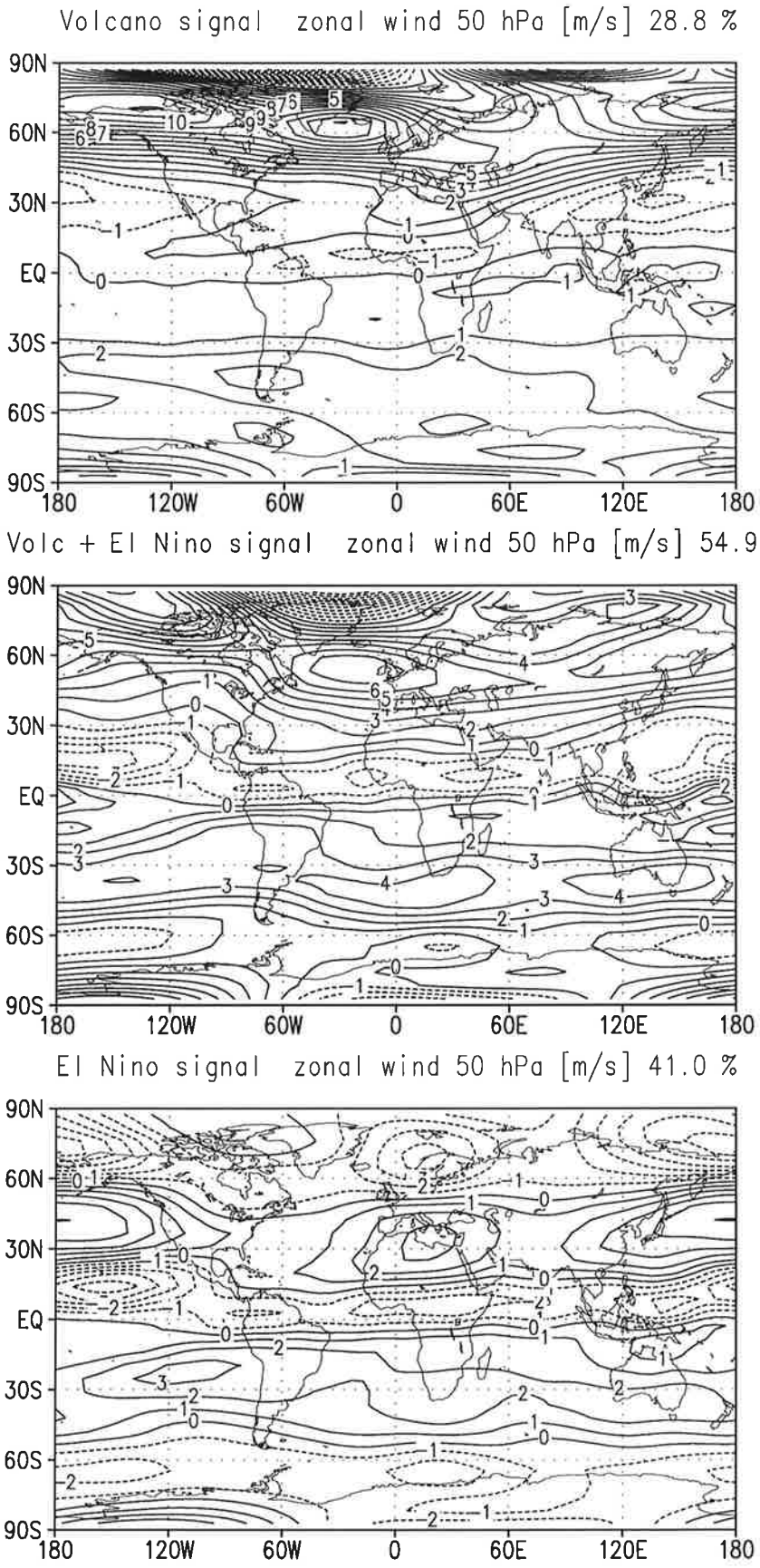

Figure 11. *The EOF filtered signal of the zonal wind in the 50 hPa level (panels see Fig. 8)*

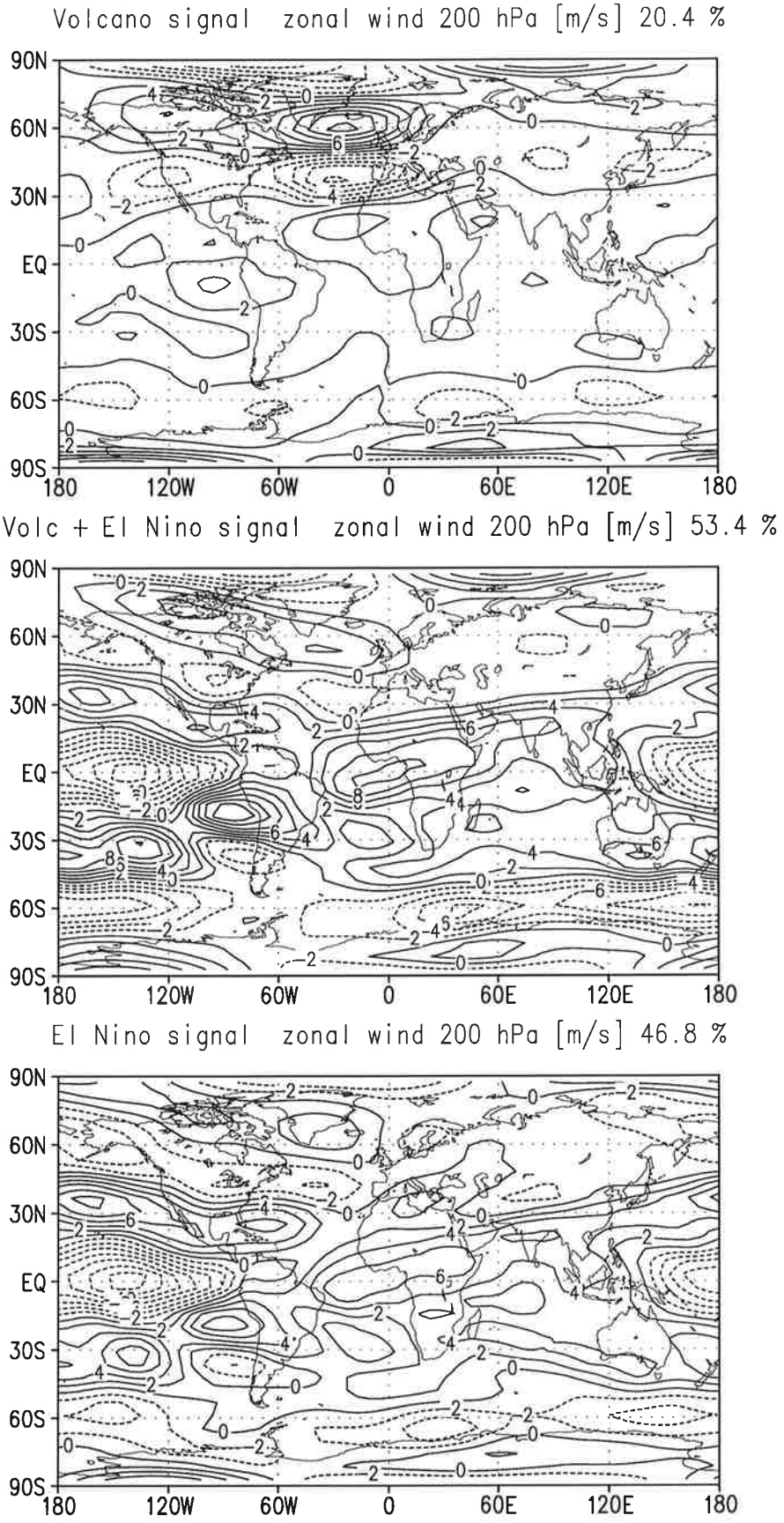

Figure 12. *The EOF filtered signal of the zonal wind in the 200 hPa level (panels see Fig. 8)*

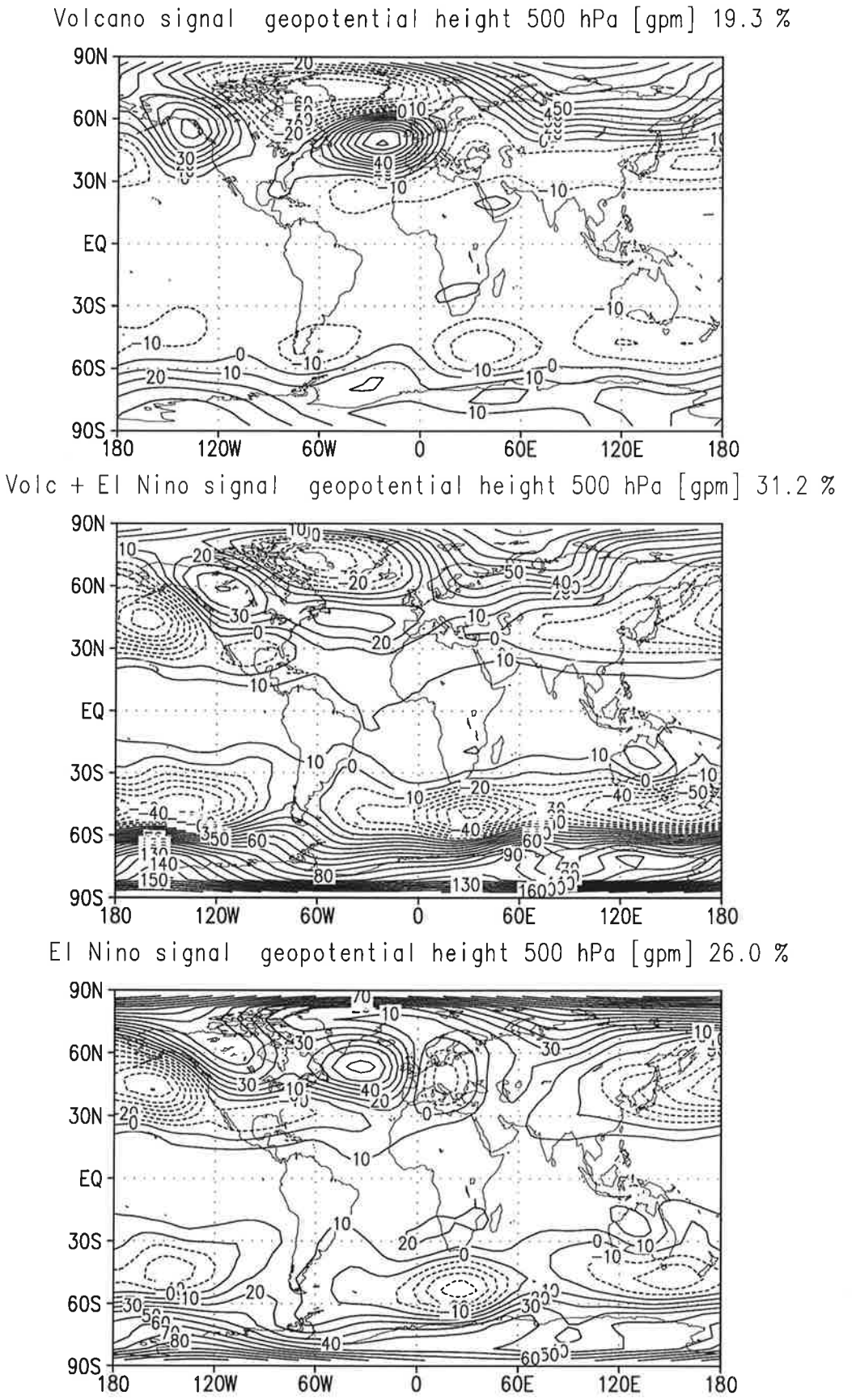

Figure 13. *The EOF filtered signal of the geopotential height of the 500 hPa level (panels see Fig. 8)*

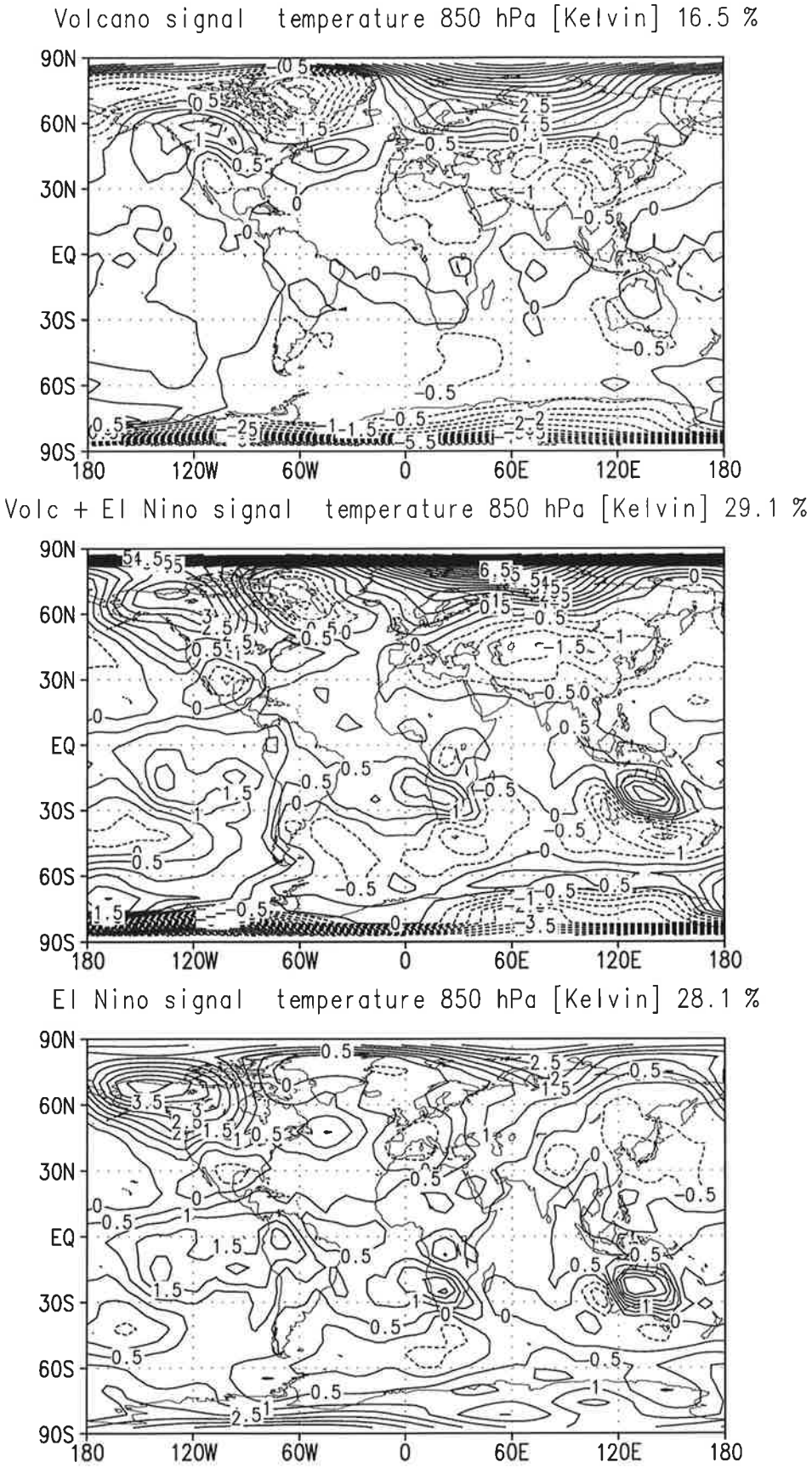

Figure 14. *The EOF filtered signal of the temperature in the 850 hPa level (panels see Fig. 8).*

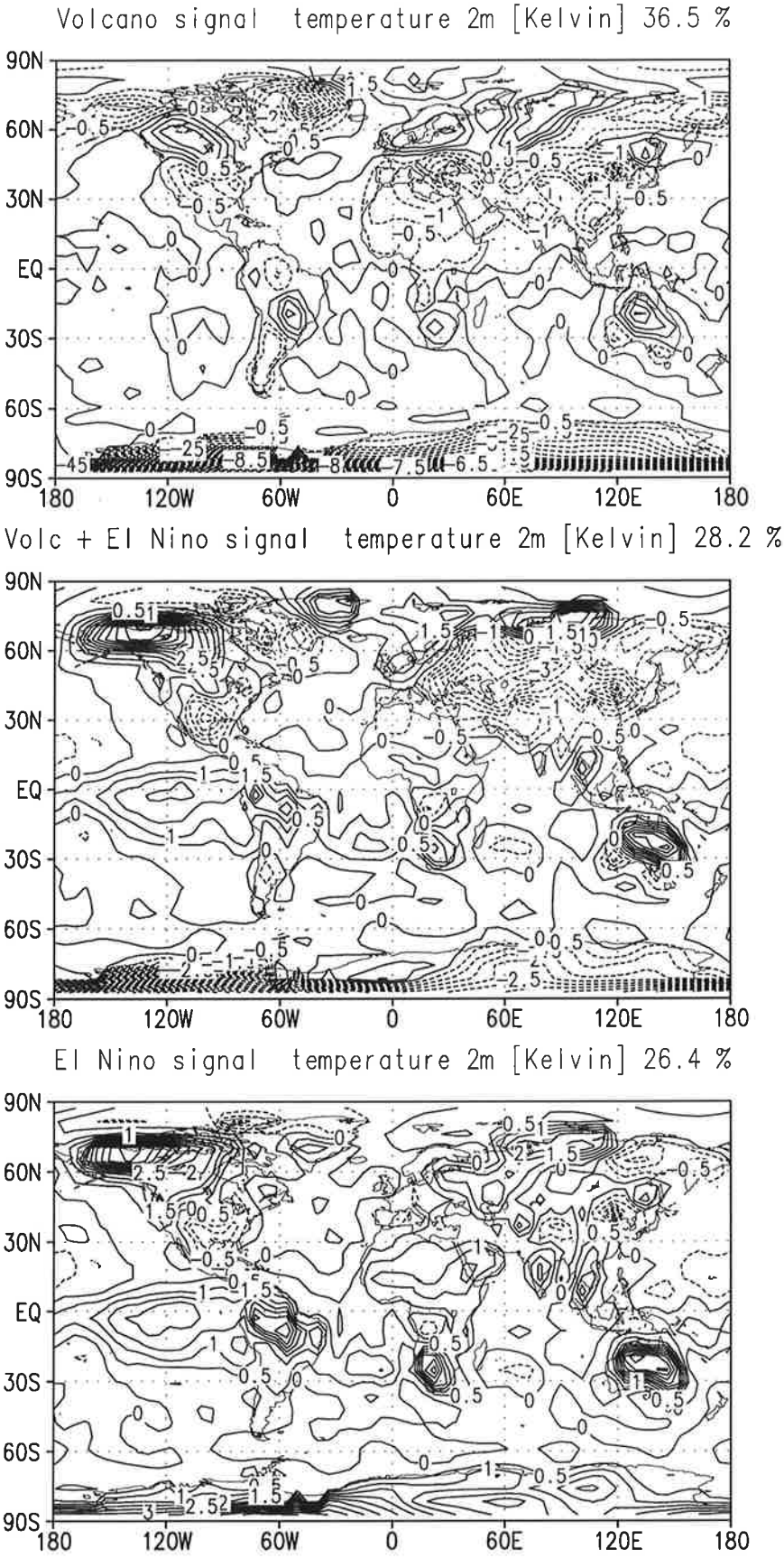

Figure 15. *The EOF filtered signal of the surface air temperature (panels see Fig. 8)*

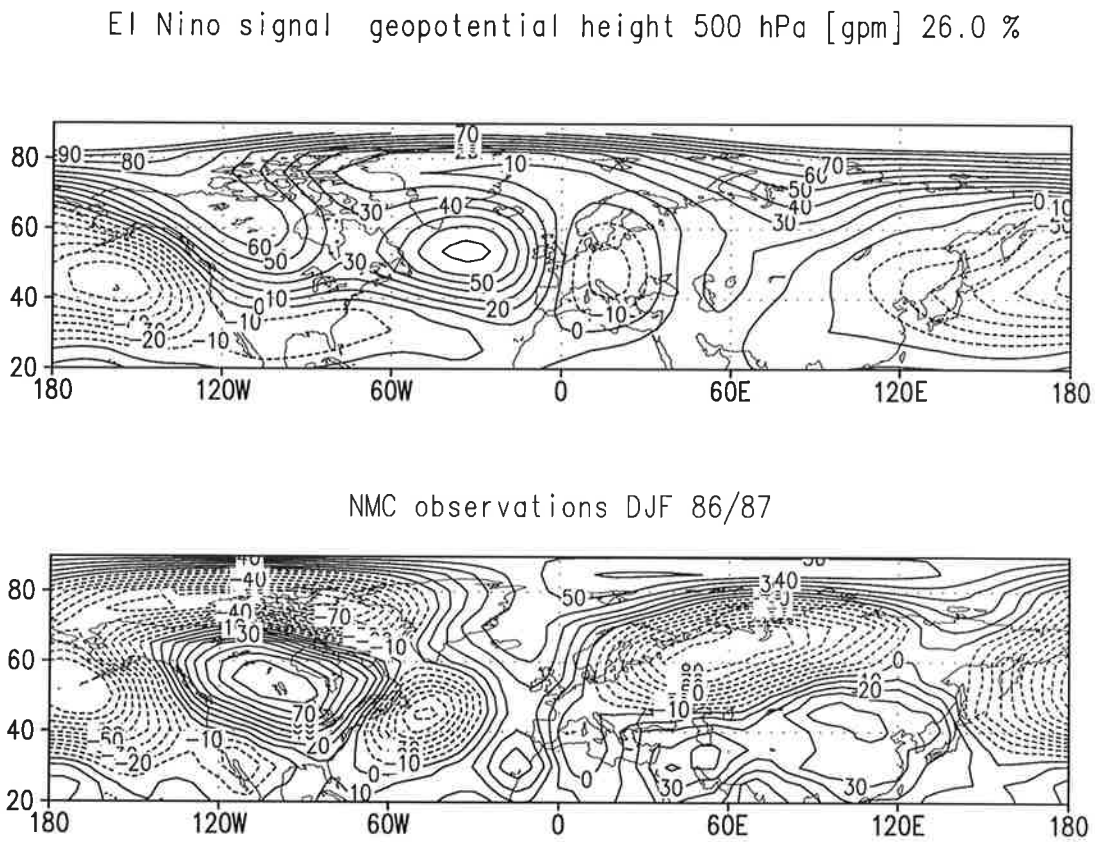

Figure 16. *The signal of the geopotential height of the 500 hPa level for the El Niño experiment (upper panel) and for observations based on NMC data for the El Niño perturbed winter 1986/87 (lower panel)*

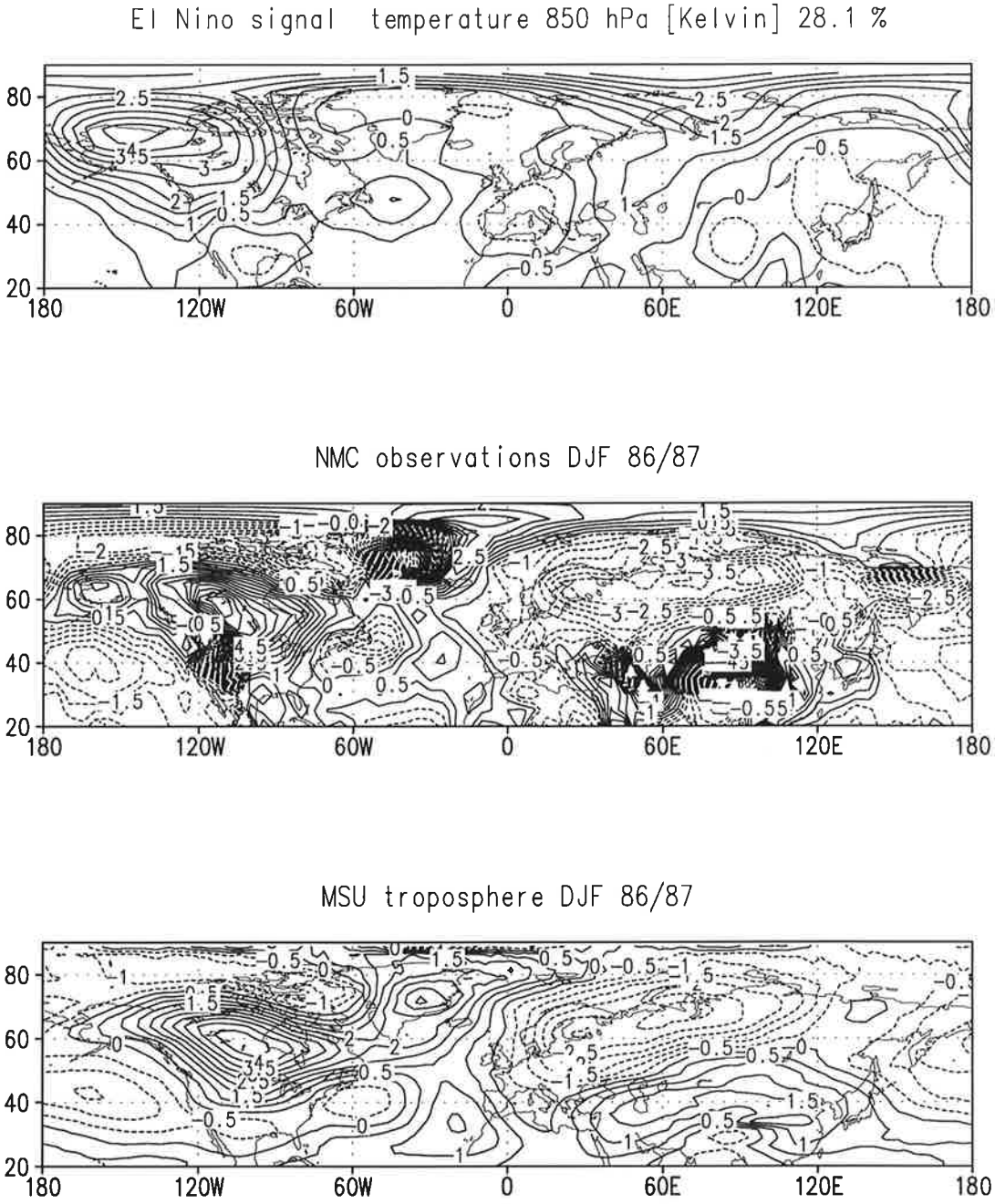

Figure 17. *The signal of the temperature in the 850 hPa level for the El Niño experiment (upper panel) and the El Niño perturbed winter of 1986/87 for two different data sets, based on NMC data (middle panel) and on MSU observations (mean 1982-1990; lower panel)*

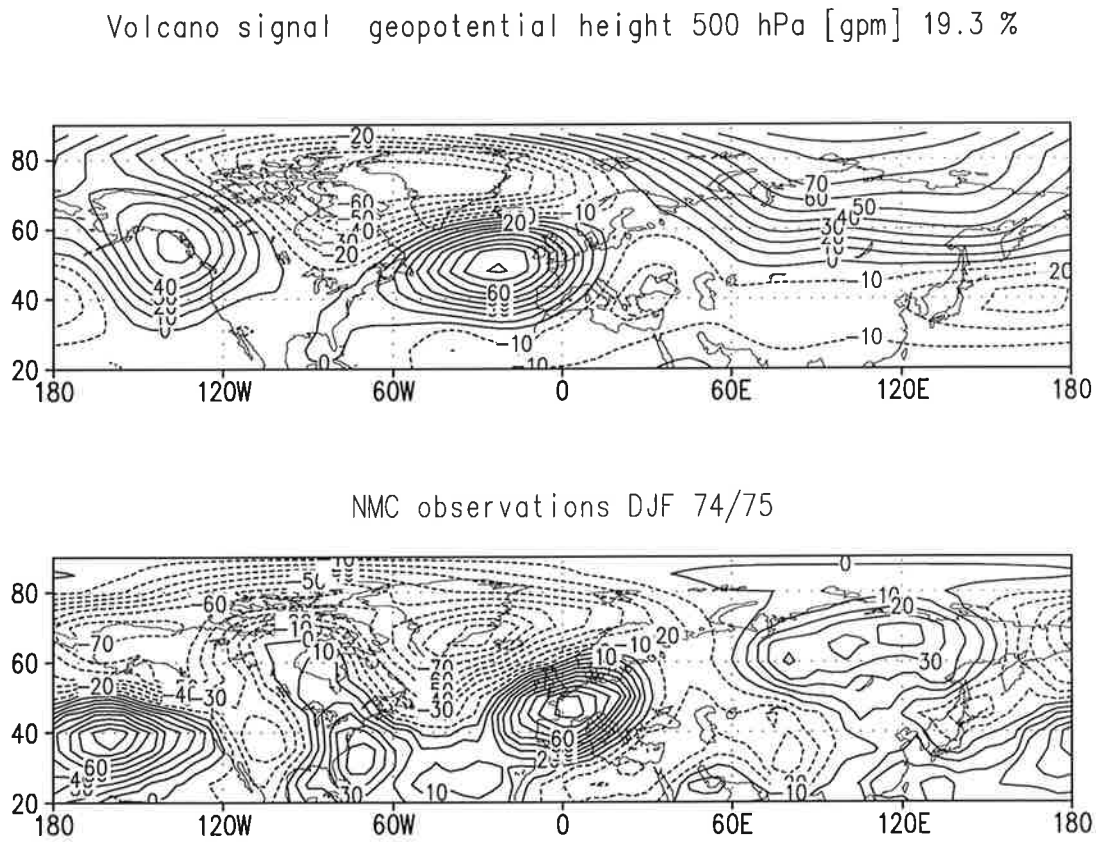

Figure 18. *The signal of the geopotential height of the 500 hPa level for the volcano experiment (upper panel) and for observations based on NMC data for the volcano perturbed winter of 1974/75 (lower panel)*

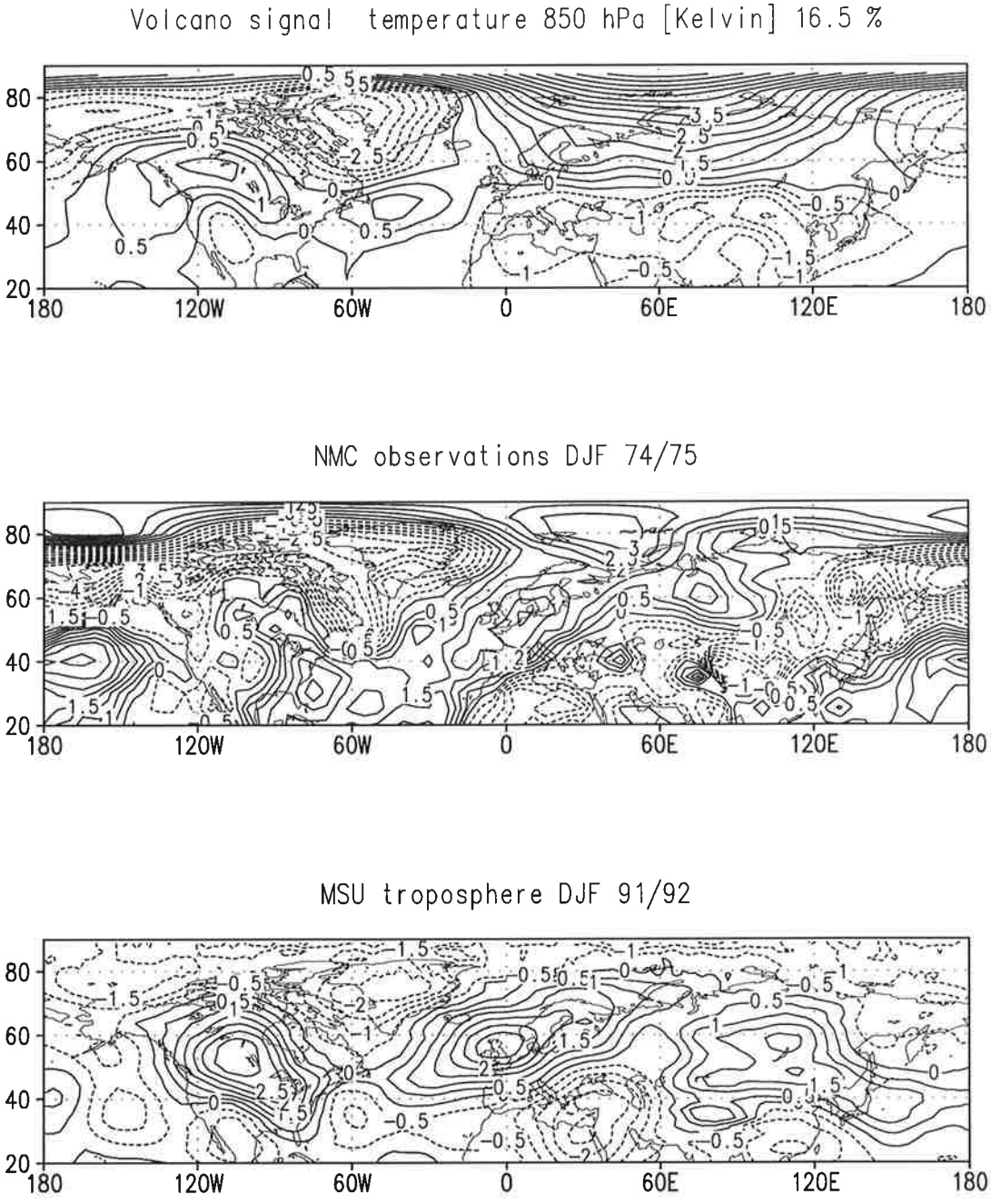

Figure 19. *The signal of the temperature in the 850hPa level for the volcano experiment (upper panel) and two different volcano perturbed winters, of 1974/75 based on NMC data (middle panel) and 1991/92 based on MSU observations (mean 1982-1990; lower panel)*

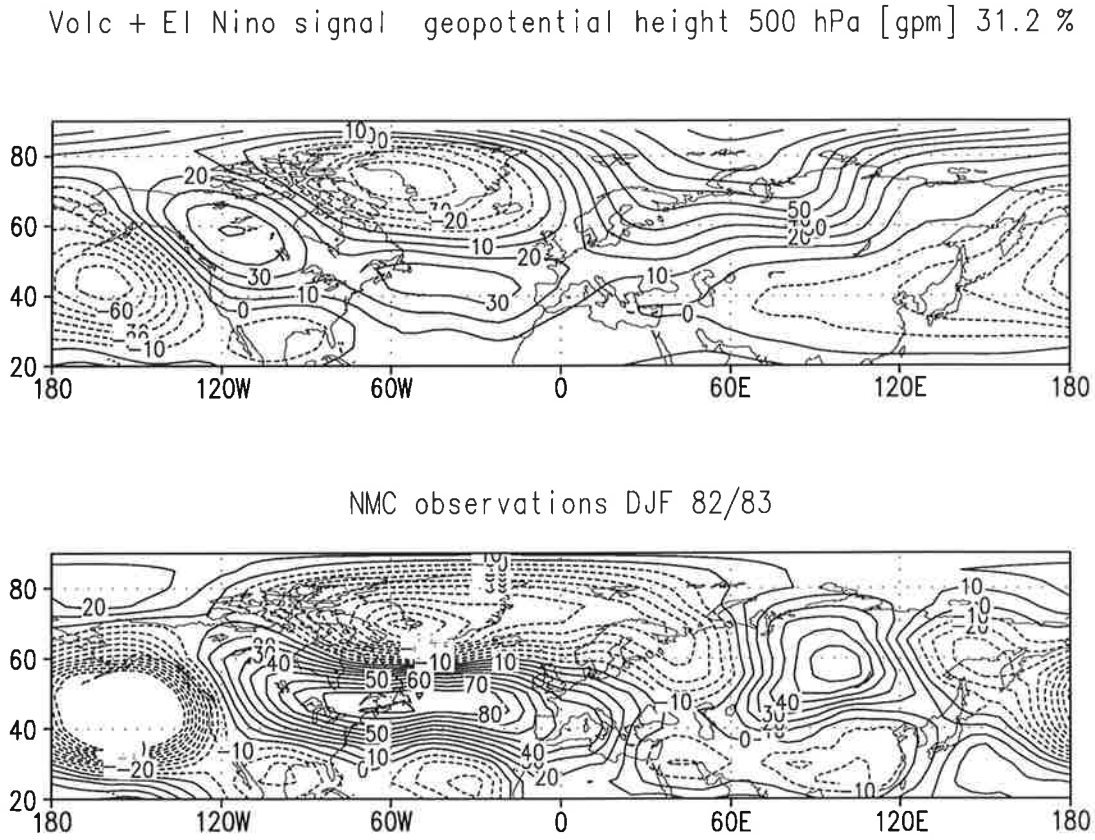

Figure 20. *The signal of the geopotential height of the 500 hPa level for the volcano / El Niño experiment (upper panel) and for observations based on NMC data for the volcano / El Niño perturbed winter of 1982 / 83 (lower panel)*

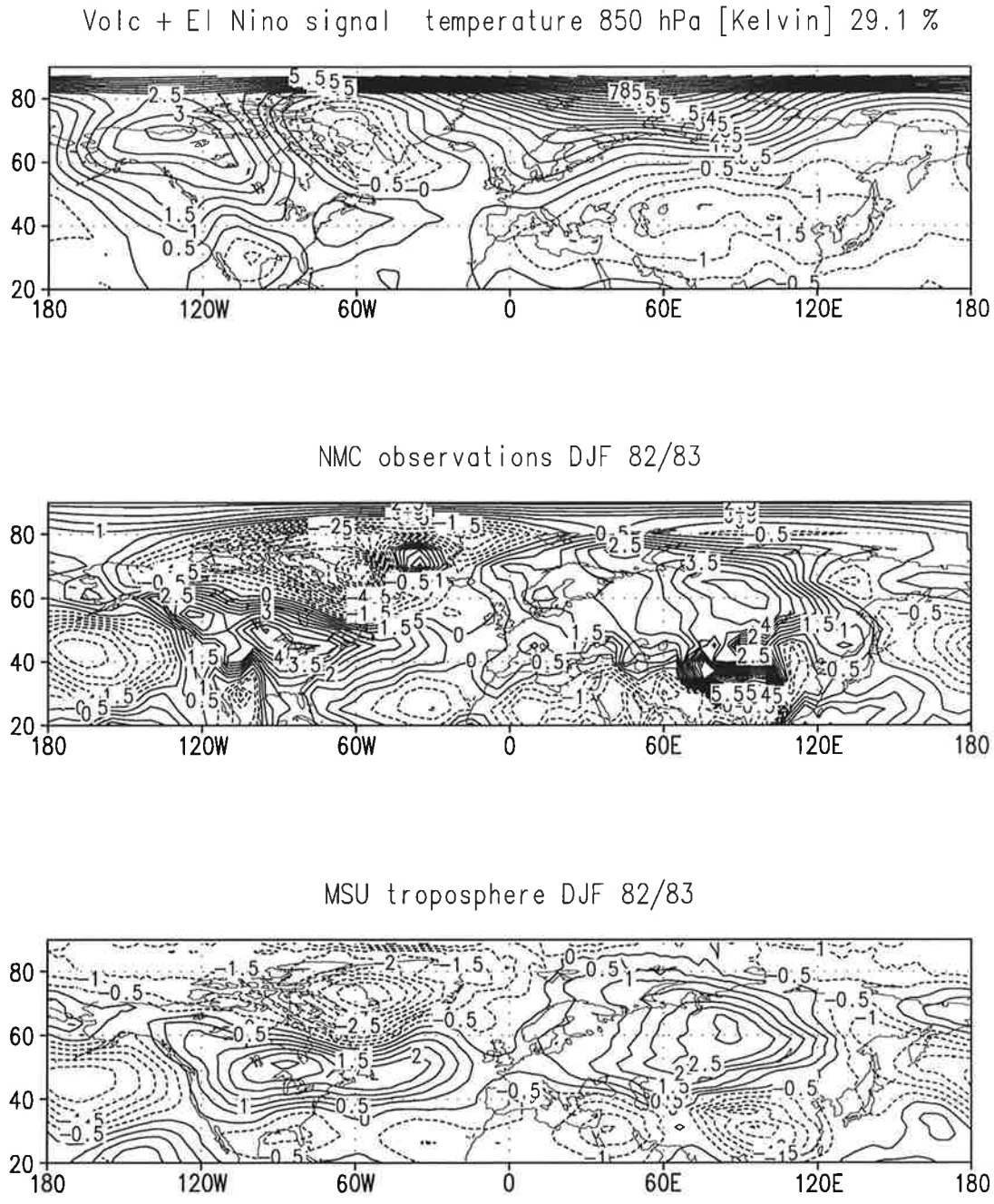

Figure 21. *The signal of the temperature in the 850hPa level for the volcano / El Niño experiment (upper panel) and the volcano / El Niño perturbed winter of 1982 / 83 for two different data sets, based on NMC data (middle panel) and on MSU observations (mean 1982-1990; lower panel)*